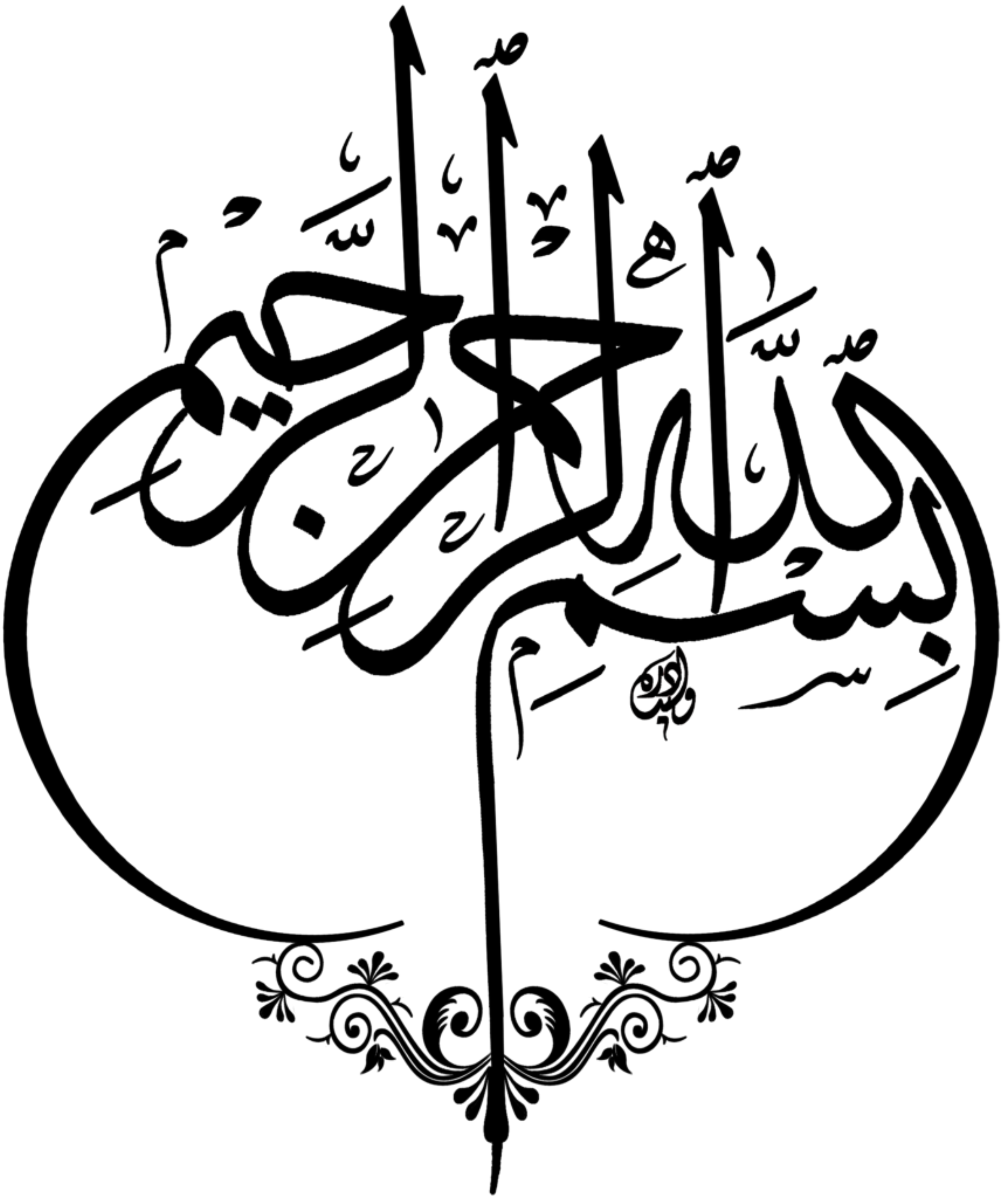

In the Name of Allah, The Most beneficiary,
The Most Gracious, The Most Merciful.

Investigation of Non-Axisymmetric Homann Stagnation-point Flow of Viscoelastic Nanofluid

By

Mahnoor Sarfraz

Department of Mathematics
Quaid-i-Azam University
Islamabad, Pakistan
2020

Investigation of Non-Axisymmetric Homann Stagnation-point Flow of Viscoelastic Nanofluid

Supervised By

Prof. Dr. Masood Khan

Department of Mathematics
Quaid-i-Azam University
Islamabad, Pakistan
2020

Investigation of Non-Axisymmetric Homann Stagnation-point Flow of Viscoelastic Nanofluid

By

Mahnoor Sarfraz

A Dissertation Submitted in the Partial Fulfillment of the Requirement for the Degree of

MASTER OF PHILOSOPHY

IN

MATHEMATICS

Supervised By

Prof. Dr. Masood Khan

Department of Mathematics
Quaid-i-Azam University
Islamabad, Pakistan
2020

Investigation of Non-Axisymmetric Homann Stagnation-point Flow of Viscoelastic Nanofluid

By

Mahnoor Sarfraz

CERTIFICATE

A DISSERTATION SUBMITTED IN THE PARTIAL FULFILLMENT OF THE REQUIREMENTS FOR THE DEGREE OF THE MASTER OF PHILOSOPHY IN MATHEMATICS

We accept this dissertation as conforming to the required standard

1. ____________________________
Prof. Dr. Masood Khan
(Supervisor)

2. ____________________________
Prof. Dr. Sohail Nadeem
(Chairman)

3. ____________________________
Dr. Nasir Ali
Associate Professor
Department of Mathematics
Faculty of Basics Applied Sciences
International Islamic University, Islamabad
(External Examiner)

Department of Mathematics
Quaid-i-Azam University
Islamabad, Pakistan
2020

Declaration

I hereby solemnly make the following declaration that the thesis under consideration and entitled “Investigation of Non-Axisymmetric Homann Stagnation-point Flow of Viscoelastic Nanofluid” is my own genuine effort. It has neither been copied from some other material nor has been presented elsewhere for obtaining any degree.

Mahnoor Sarfraz

Dedicated To

My mother, ***Samia Sarfraz*** and my sister, ***Wajiha Sarfraz***.
You have been with me every step of the way, through
good times and bad. Thank you for your unconditional
love, guidance, trust and instilling in me the confidence
that I can do anything I put my mind to.
Thank you for everything guys!

Acknowledgement

All praise be to ***ALLAH*** Almighty, the most Eternal and the Majestic, Who created me, inculcated the dedication and strength in me to complete this thesis. My words are not enough to express my gratitude to Him. I offer my sincerest gratitude to the Holy Prophet ***Muhammad*** (Peace be upon Him), who had guided the mankind from the darkness to the prestigious age of civilization.

My heartful thanks to all my teachers who has enabled me today to face this scholastic zenith. I cordially appreciate the kindness, endless support, devoted efforts and precious time of my advisor-mentor, **Professor Dr. *Masood Khan***, who has directed me with his rational suggestions and constructive criticism. I deem without his encouragement my abilities incommensurate to the assigned work. I am highly indebted and obliged to him ever.

I gratefully acknowledge my respectable lab fellows **Mr. *Jawad Ahmed,*** **Mr. *Awais Ahmed*** and **Mr. *Wajid Ali*** for their logical ideas, unstinting and unwavering support. They always responded to my queries with enthusiasm and concern.

I am grateful to **Dr. *Constantin Fetecau*** from Academy of Romanian Scientists, Bucuresti, Romania for his constructive comments on Chapter 2 of this thesis.

I owe my indebtedness to my family, especially my mother, ***Samia Sarfraz*** and sister ***Wajiha Sarfraz,*** who have provided me financial and moral support in every step of life and motivated me to achieve my goals. Without your assistance and love, I am nothing. You both have been my best cheerleaders. All that I am, I owe it to my mother.

Finally, I extend my warm thanks to my friends, ***Sana Tahir*** and ***Huma Jamil*** for their unfathomable friendship and moral support throughout this journey.

Mahnoor Sarfraz

List of Abbreviations

- **2D:** Two-Dimensional
- **3D:** Three-Dimensional
- **BVP:** Boundary Value Problem
- **BL:** Boundary Layer
- **MHD:** Magnetohydrodynamic
- **NS:** Navier-Stokes
- **ODEs:** Ordinary Differential Equations

Preface

Non-Newtonian fluids (polymeric liquids) have remarkable significance in nearly every field, industry and technology. Their study is of eclectic interest for many researcher, engineers and mathematicians. They form an extensive range of products scilicet molten polymers, paints, thermoplastics, starch suspension, and so forth, that do not obey Newton's law of viscosity. Before-mentioned fluids obey the power-law model, which explains that stress functions nonlinearly with the deformation rate. The constitutive equations with the corresponding stress tensor are determined to model their viscoelastic conduct. Moreover, the investigation of flows in the stagnation zone is another fascinating area of study in fluid mechanics. This is because of the superfluous pressure and heat transport in the stagnation region, it is reckoned amongst the intriguing intricacies and has multiple applications as well.

The present study highlights the modification of Homann's problem for the viscoelastic fluids adjacent to the stagnation region over a cylindrical disk with a time-independent free stream. By superposing periodic radial and azimuthal velocity terms onto Homann's external potential flow, the potential flow field in the cylindrical coordinates system is attained. This directs us to a distinct class of asymmetric flow near the stagnation-point, which solely depends upon shear-to-strain rate ratio. Furthermore, the impression of non-axisymmetry and magnetohydrodynamic (MHD) on Walter’s B liquid and Jeffrey fluid flow is inspected. Additionally, to highlight the nanofluid conduct, we employed the Buongiorno model. The outcomes of the pertinent parameters on the boundary layer are also scrutinized. The conservation laws are remodeled by a similarity transformation. A collocation method, specifically bvp4c is employed to numerically compute the solutions. A comparison is made between the numerical and their asymptotic outcomes for large values of shear-to-strain rate ratio. The outcomes of viscoelasticity and magnetic field on the skin friction and displacement thicknesses are also determined by perturbative expansion.

This thesis is comprised of three Chapters. Chapter 1 addresses the conservation laws, definitions, and stress tensors related to the non-Newtonian fluids discussed in the succeeding chapters, literature survey, and the procedure to determine the solution for the problems. Chapter 2 explores the non-axisymmetric Homann flow of Walter's B nanofluid model along with non-linear Rosseland thermal radiation. Chapter 3

includes the study of Jeffrey's nanofluid in the stagnation-region with an electrically conducting flow. For both the problems, it is concluded that when the shear-to-strain-rate ratio approaches infinity, the coefficient of skin friction along *x*-direction reaches its asymptotic behavior; however, along *y*-direction it shows contrary results. Further conclusions are jotted down at the end of chapters 2 and 3.

Contents

Chapter 1

Literature Survey and Preliminaries

This chapter aims to address the fundamental laws, definitions related to the non-Newtonian fluids, literature survey and the procedure to determine the solution for the problems which are scrutinized in the following chapters.

1.1 Continuum Mechanics and its Branches

Continuum Mechanics deals with the study of kinematics and mechanisms of substances, that have continuous mass distribution rather than discrete. It has two divisions; solid mechanics and fluid mechanics. The former explains the behavioral study of solid bodies, particularly their kinematic and mechanical properties. The latter depicts the kinematics and mechanical features of remaining states of matter, *i.e.*, liquid, gas, and plasma, which deforms regularly when a shear force is applied. Fluid mechanics is further subdivided into two branches; fluid dynamics (the study of moving fluid) and fluid statics (the study of stationary fluid).

1.2 Characteristics of Fluid

Every fluid (liquid, gas and plasma) has some peculiar properties that are slightly the same in others, particularly, their density, viscosity, pressure, specific heat capacity, shear stress, and so forth. Some of their significant properties are addressed here.

1.2.1 Shear Stress

Shear stress $\boldsymbol{\tau}$ is the tendency to deform a state of fluid as a result of an applied stress. The coefficient of wall shear stress $C_{\breve{f}}$ is also known as *skin friction*, which is the resistance between the fluid layers, and given as $C_{\breve{f}} \propto \boldsymbol{\tau}$.

1.2.2 Density

Mass density ρ is a crucial property of any fluid. It specifies either a body placed in a fluid floats or not, and is interpreted as "the quantity of matter in a space" at a particular value of temperature or applied force.

1.2.3 Viscosity

Viscosity is the friction or resisting strength against the fluid motion. Under specified conditions, it can be incorporated with the deformation rate of fluid molecules against the force applied or temperature distribution. It solely depends on the state of matter which is under consideration, that is for liquid viscosity reduces when the temperature is elevated; however, in gases, it enhances by raising the temperature of the system. It is divided into two types; dynamic/absolute μ and kinematic viscosity ν. Former links shear-stress $\boldsymbol{\tau}$ with strain-rate γ, *i.e.*, $\mu = \frac{\boldsymbol{\tau}}{\gamma}$; whilst, latter associates the relation between absolute viscosity μ and density ρ of the fluid, given as $\nu = \frac{\mu}{\rho}$.

1.3 Classification of Fluids

Fluids are divided into different categories based on their physical and mechanical attributes.

1.3.1 Inviscid Fluids

Fluids having no interfacial or surface tension and viscosity $\mu = 0$ are identified as inviscid or *ideal*. Such fluids are also incompressible, *i.e.*, $\boldsymbol{\nabla} \cdot \mathbf{V} = 0$ and irrotational in nature. Under specific engineering practices, some fluids exhibit no coherence impact and loss of kinetic energy, thus they are handled as an ideal, e.g., superfluids.

1.3.2 Real Fluids

Fluids with non-zero viscosity $\mu \neq 0$ and interfacial or surface tension deform in a continuous manner are termed as *real*.

1.3.3 Nanofluids

Base-fluids comprising suspended nanometer structured particles are termed as *nanofluids*, where base-fluids are mostly comprised of water, some intricate compounds of hydrocarbons fluids, *i.e.*, Ethylene glycol and crude oil (nano-lubricants).

1.4 Newtonian vs Non-Newtonian Fluid

1.4.1 Newtonian Fluids

Fluids that follows Newton's viscous law are termed as *Newtonian.* Such fluids depict the linearity between the shear stress and the deformation rate, e.g., all viscous and ideal fluids.

$$\boldsymbol{\tau}_{yx} = \mu \frac{\partial \breve{u}}{\partial y}, \tag{1.1}$$

where $\frac{\partial \breve{u}}{\partial y}$, μ, and $\boldsymbol{\tau}_{yx}$ represent the deformation rate, absolute viscosity, and shear stress, respectively.

1.4.2 Non-Newtonian Fluids

Fluids with variable viscosity are categorized as non-Newtonian (polymeric liquids). They obey the *power-law model*, which explains the non-linearity among the stress and deformation (shear) rate. Because of their intricate relation between stress and stain, rheological characteristics, they exhibit Weissenberg effect. They form an extensive range of products, e.g., molten polymers, paints, starch suspension, thermoplastics, and so forth, that do not exhibit Newtonian properties.

$$\boldsymbol{\tau}_{yx} = \kappa \left(\frac{\partial \breve{u}}{\partial y} \right)^{N}, \tag{1.2}$$

where the index κ represents relative consistency and N determine nature of the fluid flow. Newtonian model given in Eq. (1.1) is retrieved when $N = 1$ and index of relative consistency κ is equal to absolute viscosity μ. Such fluids are classified into categories depending upon their characteristics; time-dependent fluids (Rheopectic and Thixotropic), viscoelastic fluids (Maxwell fluid, Oldroyd fluid, etc), and time-independent fluids (Dilatant, Bingham-plastic, and Pseudoplastic).

1.5 Flow and Heat Transfer Analysis

In this section, the boundary layer approximation for the flow analysis and methods of heat transport are addressed.

1.5.1 Boundary Layer Flow

Ludwig Prandtl did a significant contribution to the subject of fluid flow by introducing the notion of the boundary layer flow. The assumptions made can lessen the complexity of the NS equation. The theory addresses such a very thin layer where the influence of viscosity is noteworthy and is in the adjacent neighborhood of the respective bounding surface called *the frictional/shear/boundary layer* (BL). According to his theory, the fluid will not slip but sticks to the wall of the surface considered. The *BL thickness* $\breve{\delta}$ is distance from the wall to boundary where the flow velocity is 99% of free-stream or far-field velocity $\breve{U}_\infty$. For further analysis scale is assumed as $\breve{\delta} \ll x \sim l$ and $\breve{\delta} \ll y \sim l$ with the similar order $\mathcal{O}$ for velocity components $\breve{u}$ and $\breve{v}$. Here l is length of a surface under consideration, and the magnitudes of velocities are equivalent to the velocity at free-stream. The scale along z-direction is assumed to be very small, whose order is equivalent to $\breve{\delta}$. The assumptions made can be written as:

$$\left.\begin{aligned} x = \mathcal{O}(1),\ \breve{u} = \mathcal{O}(1), \\ y = \mathcal{O}(1),\ \breve{v} = \mathcal{O}(1), \\ z = \mathcal{O}(\breve{\delta}),\ \breve{w} = \mathcal{O}(\breve{\delta}), \end{aligned}\right\} \tag{1.3}$$

where $\mathcal{O}$ is a *Landau's symbol* which represents growth-rate or order of a function.

1.5.2 Modes of Heat Transfer

Heat can transport from one body to another by following fundamental methods.

Conduction

The method in which heat is transported without actual motion of the particles, but due to the vibration of molecules in contact, is known as the *diffusion* or conduction. It is best examined in solids and metals such as copper and gold because of their structural advantage have great conductivity, such elements that have free electrons and are known as conductors, while those who negate these properties are called insulators. Fourier's law is generally practiced to compute the thermal conductivity of any matter.

Convection

The method in which heat is transported from warmer to cooler regions in a fluid is known as convection. Convection is accurately observed in fluids due to their structural difference with solids as heat transportation is caused by mass transfer or motion of particles.

Radiation

The method in which heat is transported in a form of waves and doesn't demand any medium for transportation is defined as radiation. It is based on *Stefan-Boltzmann law.* This process does not depend on any connection among the source of heat or body to be heated. A well-known example is the emission of heat rays from the sun (in a form of light waves).

1.6 Conservation Laws

1.6.1 Continuity Principle

The equation of continuity is also identified as *mass conservation principle*, which states that within an isolated system mass of a body is constant throughout a chemical reaction or physical conversion, *i.e.*, mass is conserved. For a compressible fluid the differential form of the equation is:

$$\frac{\partial \rho}{\partial t} + \operatorname{div}(\rho \mathbf{V}) = 0. \tag{1.4}$$

Since density ρ is constant for an incompressible fluid, therefore the above relation is reduced as:

$$\boldsymbol{\nabla} \cdot \mathbf{V} = 0. \tag{1.5}$$

This equation expresses the fluid flow, such as blood flow rate in vessels, arteries, and veins.

1.6.2 Momentum Equation

Momentum equation or *momentum conservation law* stems from principle that the momentum in an isolated system is unchanged. By acknowledging the impression of *Lorentz force* as body force exhibited by the magnetic field, the translational flow is directed by the momentum conservation law:

$$\rho \frac{D\mathbf{V}}{Dt} = \boldsymbol{\nabla} \cdot \boldsymbol{\tau} + \mathbf{J} \times \mathbf{B}. \tag{1.6}$$

Here$\frac{D}{Dt} \equiv \frac{\partial}{\partial t} + \mathbf{V} \cdot \boldsymbol{\nabla}$, $\boldsymbol{\tau} = -p\mathbf{I} + \mathbf{S}$ and $\mathbf{J} = (\mathbf{V} \times \mathbf{B})\,\sigma + \mathbf{E}\sigma$, is the material derivative, the stress tensor with $\mathbf{S}$ the extra/true-stress tensor, and the current density, respectively. The term $(\mathbf{V} \times \mathbf{B})\,\sigma$ the magnetic field and $\mathbf{E}\sigma$ represents the electric field. For $\mathbf{E} = 0$, the Lorentz force is given as:

$$\mathbf{J} \times \mathbf{B} = (\mathbf{V} \times \mathbf{B})\,\sigma \times \mathbf{B}. \tag{1.7}$$

The investigation of such flows is a well-known subject of interest for many researchers named magnetohydrodynamics (MHD).

1.6.3 Energy Equation

The heat transfer analysis is performed by the *energy conservation principle*, which is correlated with the first thermodynamics law. Since the thesis covers the problem modeled for nanofluid flow studied by adopting Buongiorno model and involving the contributions of non-linear Rosseland radiation, the energy equation is given as:

$$(\rho c)_p \frac{D\breve{T}}{Dt} = k_{nf}\boldsymbol{\nabla}^2\breve{T} + (\rho c)_{nf}\left[D_B\boldsymbol{\nabla}\breve{C}\cdot\boldsymbol{\nabla}\breve{T} + D_T\frac{\boldsymbol{\nabla}\breve{T}\cdot\boldsymbol{\nabla}\breve{T}}{\breve{T}_\infty}\right] - \boldsymbol{\nabla}\cdot q_T, \tag{1.8}$$

where c_p, $\breve{T}$, k_{nf}, $\breve{C}$, D_B, D_T, $\breve{T}_\infty$, and q_T represent the specific heat, the fluid temperature, thermal conductivity parameter, the fluid concentration, the mass or Brownian diffusion coefficient, the thermophoretic coefficient, the ambient fluid temperature, and the thermal heat-flux (given by Fourier's law), respectively.

1.6.4 Mass Transport Equation

The mass transport inquiry is done by the nanoparticle concentration conservation law (represented by Fick's law). By selecting Buongiorno model for nanofluid, the concentration distribution is expressed as:

$$\frac{D\breve{C}}{Dt} = \boldsymbol{\nabla}\cdot\left[D_B\boldsymbol{\nabla}\breve{C} + \frac{D_T}{\breve{T}_\infty}\boldsymbol{\nabla}\breve{T}\right]. \tag{1.9}$$

1.7 Mathematical Models

1.7.1 Walter's B Liquid Model

This model explicitly covers the perplexing characteristic of many industrial fluids and their elastic properties. The system of equations generated by the true-stress tensor is extremely nonlinear in nature. The Cauchy's tensor $\boldsymbol{\tau}_{ab}$ in Cartesian coordinate is stated with the strain-rate tensor e_{ab} as:

$$\boldsymbol{\tau}_{ab} = -p\delta_{ab} + 2\mu e_{ab} - 2k_0\left[\frac{\partial e_{ab}}{\partial t} + v_c\frac{\partial e_{ab}}{\partial x_c} - e_{ac}\frac{\partial v_b}{\partial x_c} - e_{cb}\frac{\partial v_a}{\partial x_c}\right], \tag{1.10}$$

where the subscript in Eq. (1.10) are $a, b, c \,\epsilon\, \{1, 2, 3\} \subseteq \mathbb{Z}^+$, $\mathbf{V} = [\breve{u}, \breve{v}, \breve{w}]$ is the velocity field, p the fluid pressure, k_0 the elastic coefficient, μ the dynamic viscosity, the strain-rate tensor $e_{ab} = \frac{1}{2}\left(\frac{\partial v_a}{\partial xb} + \frac{\partial vb}{\partial x_a}\right)$ and $\delta_{ab} = \begin{cases} 1 \text{ when } a = b \\ 0 \text{ when } a \neq b \end{cases}$ is Kronecker Delta.

The components of stress tensor in Cartesian coordinate system for steady are given below.

$$\begin{aligned}\tau_{11} = -p + 2\mu\frac{\partial \breve{u}}{\partial x} - 2k_0 \bigg[& \breve{u}\frac{\partial^2 \breve{u}}{\partial x^2} + \breve{v}\frac{\partial^2 \breve{u}}{\partial x \partial y} + \breve{w}\frac{\partial^2 \breve{u}}{\partial x \partial z} - 2\left(\frac{\partial \breve{u}}{\partial x}\right)^2 \\ & -\frac{\partial \breve{u}}{\partial y}\left(\frac{\partial \breve{v}}{\partial x} + \frac{\partial \breve{u}}{\partial y}\right) - \frac{\partial \breve{u}}{\partial z}\left(\frac{\partial \breve{w}}{\partial x} + \frac{\partial \breve{u}}{\partial z}\right)\bigg],\end{aligned} \tag{1.11}$$

$$\begin{aligned}\tau_{22} = -p + 2\mu\frac{\partial \breve{v}}{\partial y} - 2k_0 \bigg[& \breve{u}\frac{\partial^2 \breve{v}}{\partial x \partial y} + \breve{v}\frac{\partial^2 \breve{v}}{\partial y^2} + \breve{w}\frac{\partial^2 \breve{v}}{\partial y \partial z} - 2\left(\frac{\partial \breve{v}}{\partial y}\right)^2 \\ & -\frac{\partial \breve{v}}{\partial x}\left(\frac{\partial \breve{v}}{\partial x} + \frac{\partial \breve{u}}{\partial y}\right) - \frac{\partial \breve{v}}{\partial z}\left(\frac{\partial \breve{w}}{\partial y} + \frac{\partial \breve{v}}{\partial z}\right)\bigg],\end{aligned} \tag{1.12}$$

$$\begin{aligned}\tau_{33} = -p + 2\mu\frac{\partial \breve{w}}{\partial z} - 2k_0 \bigg[& \breve{u}\frac{\partial^2 \breve{w}}{\partial x \partial z} + \breve{v}\frac{\partial^2 \breve{w}}{\partial y \partial z} + \breve{w}\frac{\partial^2 \breve{w}}{\partial z^2} - 2\left(\frac{\partial \breve{w}}{\partial z}\right)^2 \\ & -\frac{\partial \breve{w}}{\partial x}\left(\frac{\partial \breve{w}}{\partial x} + \frac{\partial \breve{u}}{\partial z}\right) - \frac{\partial \breve{w}}{\partial y}\left(\frac{\partial \breve{w}}{\partial y} + \frac{\partial \breve{v}}{\partial z}\right)\bigg],\end{aligned} \tag{1.13}$$

$$\begin{aligned}\tau_{12} = {} & \mu\left(\frac{\partial \breve{v}}{\partial x} + \frac{\partial \breve{u}}{\partial y}\right) - 2k_0 \bigg[\frac{\breve{u}}{2}\left(\frac{\partial^2 \breve{v}}{\partial x^2} + \frac{\partial^2 \breve{u}}{\partial x \partial y}\right) + \frac{\breve{v}}{2}\left(\frac{\partial^2 \breve{u}}{\partial y^2} + \frac{\partial^2 \breve{v}}{\partial x \partial y}\right) \\ & + \frac{\breve{w}}{2}\left(\frac{\partial^2 \breve{u}}{\partial y \partial z} + \frac{\partial^2 \breve{v}}{\partial x \partial z}\right) - \frac{\partial \breve{u}}{\partial x}\frac{\partial \breve{v}}{\partial x} - \frac{1}{2}\left(\frac{\partial \breve{v}}{\partial x} + \frac{\partial \breve{u}}{\partial y}\right)\frac{\partial \breve{v}}{\partial y} - \frac{1}{2}\left(\frac{\partial \breve{w}}{\partial x} + \frac{\partial \breve{u}}{\partial z}\right)\frac{\partial \breve{v}}{\partial z} \\ & -\frac{1}{2}\left(\frac{\partial \breve{v}}{\partial x} + \frac{\partial \breve{u}}{\partial y}\right)\frac{\partial \breve{u}}{\partial x} - \frac{\partial \breve{v}}{\partial y}\frac{\partial \breve{u}}{\partial y} - \frac{1}{2}\left(\frac{\partial \breve{w}}{\partial y} + \frac{\partial \breve{v}}{\partial z}\right)\frac{\partial \breve{u}}{\partial z} = \tau_{21},\end{aligned} \tag{1.14}$$

$$\begin{aligned}\tau_{13} = {} & \mu\left(\frac{\partial \breve{w}}{\partial x} + \frac{\partial \breve{u}}{\partial z}\right) - 2k_0 \bigg[\frac{\breve{u}}{2}\left(\frac{\partial^2 \breve{w}}{\partial x^2} + \frac{\partial^2 \breve{u}}{\partial x \partial z}\right) + \frac{\breve{v}}{2}\left(\frac{\partial^2 \breve{u}}{\partial y \partial z} + \frac{\partial^2 \breve{w}}{\partial x \partial y}\right) \\ & + \frac{\breve{w}}{2}\left(\frac{\partial^2 \breve{u}}{\partial z^2} + \frac{\partial^2 \breve{w}}{\partial x \partial z}\right) - \frac{\partial \breve{u}}{\partial x}\frac{\partial \breve{w}}{\partial x} - \frac{1}{2}\left(\frac{\partial \breve{v}}{\partial x} + \frac{\partial \breve{u}}{\partial y}\right)\frac{\partial \breve{w}}{\partial y} - \frac{1}{2}\left(\frac{\partial \breve{w}}{\partial x} + \frac{\partial \breve{u}}{\partial z}\right)\frac{\partial \breve{w}}{\partial z} \\ & -\frac{1}{2}\left(\frac{\partial \breve{w}}{\partial x} + \frac{\partial \breve{u}}{\partial z}\right)\frac{\partial \breve{u}}{\partial x} - \frac{\partial \breve{w}}{\partial z}\frac{\partial \breve{u}}{\partial z} - \frac{1}{2}\left(\frac{\partial \breve{w}}{\partial y} + \frac{\partial \breve{v}}{\partial z}\right)\frac{\partial \breve{u}}{\partial z} = \tau_{31},\end{aligned} \tag{1.15}$$

$$\begin{aligned}\tau_{23} = \mu\left(\frac{\partial \breve{w}}{\partial y}+\frac{\partial \breve{v}}{\partial z}\right) - 2k_0 \Bigg[\frac{\breve{u}}{2}\left(\frac{\partial^2 \breve{v}}{\partial x \partial z}+\frac{\partial^2 \breve{w}}{\partial y \partial z}\right)+\frac{\breve{v}}{2}\left(\frac{\partial^2 \breve{w}}{\partial y^2}+\frac{\partial^2 \breve{v}}{\partial y \partial z}\right) \\ +\frac{\breve{w}}{2}\left(\frac{\partial^2 \breve{v}}{\partial z^2}+\frac{\partial^2 \breve{w}}{\partial y \partial z}\right)-\frac{1}{2}\left(\frac{\partial \breve{v}}{\partial x}+\frac{\partial \breve{u}}{\partial y}\right)\frac{\partial \breve{w}}{\partial x}-\frac{\partial \breve{v}}{\partial y}\frac{\partial \breve{w}}{\partial y}-\frac{1}{2}\left(\frac{\partial \breve{w}}{\partial y}+\frac{\partial \breve{v}}{\partial z}\right)\frac{\partial \breve{w}}{\partial z} \\ -\frac{1}{2}\left(\frac{\partial \breve{w}}{\partial x}+\frac{\partial \breve{u}}{\partial z}\right)\frac{\partial \breve{v}}{\partial x}-\frac{1}{2}\left(\frac{\partial \breve{w}}{\partial y}+\frac{\partial \breve{v}}{\partial z}\right)\frac{\partial \breve{v}}{\partial y}-\frac{\partial \breve{w}}{\partial z}\frac{\partial \breve{v}}{\partial z} = \tau_{32}.\end{aligned} \tag{1.16}$$

Here τ_{11}, τ_{22}, and τ_{33} are the diagonal entries, τ_{12}, τ_{21}, τ_{13}, τ_{31}, τ_{23}, and τ_{32}, are the non-diagonal entries tensor.

1.7.2 Jeffrey Fluid Model

The Jeffrey fluid model depicts the rheological aspects of polymer liquids by acknowledging the impact of relaxation-time and retardation-time. Highly non-linear equations are produced by the extra or true-stress tensor $\mathbf{S}$, expressed as:

$$\boldsymbol{\tau} = -p\mathbf{I} + \mathbf{S}, \text{ and } \mathbf{S} = \frac{\mu}{1+\lambda_1}\left[\mathbf{R}_1 + \lambda_2\left(\frac{\partial \mathbf{R}_1}{\partial t} + (\mathbf{V}\cdot\boldsymbol{\nabla})\,\mathbf{R}_1\right)\right], \tag{1.17}$$

where $\boldsymbol{\tau}$ is the Cauchy tensor, $\mathbf{V} = [\breve{u}, \breve{v}, \breve{w}]$, λ_1, and λ_2, are the velocity field, the relaxation-to-retardation times ratio, the retardation time, respectively. $\mathbf{R}_1$ is the first-order *Rivlin-Ericksen tensor* given as $\mathbf{R}_1 = \operatorname{grad}\mathbf{V} + (\operatorname{grad}\mathbf{V})^T$. For steady case 3D flow, the extra-stress tensor $\mathbf{S}$ in Cartesian coordinate system in terms of components is given as:

$$S_{11} = \frac{\mu}{1+\lambda_1}\left[2\frac{\partial \breve{u}}{\partial x} + \lambda_2\left(\breve{u}\frac{\partial}{\partial x}+\breve{v}\frac{\partial}{\partial y}+\breve{w}\frac{\partial}{\partial z}\right)\left(2\frac{\partial \breve{u}}{\partial x}\right)\right], \tag{1.18}$$

$$S_{22} = \frac{\mu}{1+\lambda_1}\left[2\frac{\partial \breve{v}}{\partial y} + \lambda_2\left(\breve{u}\frac{\partial}{\partial x}+\breve{v}\frac{\partial}{\partial y}+\breve{w}\frac{\partial}{\partial z}\right)\left(2\frac{\partial \breve{v}}{\partial y}\right)\right], \tag{1.19}$$

$$S_{33} = \frac{\mu}{1+\lambda_1}\left[2\frac{\partial \breve{w}}{\partial z} + \lambda_2\left(\breve{u}\frac{\partial}{\partial x}+\breve{v}\frac{\partial}{\partial y}+\breve{w}\frac{\partial}{\partial z}\right)\left(2\frac{\partial \breve{w}}{\partial z}\right)\right], \tag{1.20}$$

$$S_{12} = \frac{\mu}{1+\lambda_1}\left[\left(\frac{\partial \breve{v}}{\partial x}+\frac{\partial \breve{u}}{\partial y}\right) + \lambda_2\left(\breve{u}\frac{\partial}{\partial x}+\breve{v}\frac{\partial}{\partial y}+\breve{w}\frac{\partial}{\partial z}\right)\left(\frac{\partial \breve{v}}{\partial x}+\frac{\partial \breve{u}}{\partial y}\right)\right] = S_{12}, \tag{1.21}$$

$$S_{13} = \frac{\mu}{1+\lambda_1}\left[\left(\frac{\partial \breve{w}}{\partial x}+\frac{\partial \breve{u}}{\partial z}\right) + \lambda_2\left(\breve{u}\frac{\partial}{\partial x}+\breve{v}\frac{\partial}{\partial y}+\breve{w}\frac{\partial}{\partial z}\right)\left(\frac{\partial \breve{w}}{\partial x}+\frac{\partial \breve{u}}{\partial z}\right)\right] = S_{13}, \tag{1.22}$$

$$S_{23} = \frac{\mu}{1+\lambda_1}\left[\left(\frac{\partial \breve{v}}{\partial z}+\frac{\partial \breve{w}}{\partial y}\right) + \lambda_2\left(\breve{u}\frac{\partial}{\partial x}+\breve{v}\frac{\partial}{\partial y}+\breve{w}\frac{\partial}{\partial z}\right)\left(\frac{\partial \breve{v}}{\partial z}+\frac{\partial \breve{w}}{\partial y}\right)\right] = S_{23}. \tag{1.23}$$

Here S_{11}, S_{22}, and S_{33} are the diagonal entries, S_{12}, S_{21}, S_{13}, S_{31}, S_{23}, and S_{32}, are the non-diagonal entries of the extra-stress tensor $\mathbf{S}$.

1.8 Non-dimensional Quantities

1.8.1 Prandtl Number

It is a non-dimensional quantity, recognized after Ludwig Prandtl. It is the ratio between the momentum-to-thermal diffusivity, given as:

$$\mathrm{Pr} = \frac{\nu}{\alpha}. \tag{1.24}$$

Here $\nu = \frac{\mu}{\rho}$, $\alpha = \frac{k}{\rho c_p}$, μ, ρc_p, and k are the momentum diffusivity, thermal diffusivity, dynamic viscosity, the volumetric heat capacity, and thermal conductivity, respectively.

1.8.2 Schmidt Number

It is a non-dimensional quantity, identified after E.H. Wilhelm Schmidt. It is the fraction between the momentum-to-mass diffusivity, given as:

$$Sc = \frac{\nu}{D_B}. \tag{1.25}$$

Here $\nu = \frac{\mu}{\rho}$, D_B, μ, and ρ are the momentum/kinematic viscosity, the mass diffusivity or Brownian diffusion coefficient, the dynamic viscosity, and the fluid density, respectively.

1.8.3 Viscoelastic Parameter

The property of substances that experiences viscous and elastic qualities during deformation is described as viscoelasticity. The parameter which depict the before-mentioned conduct of a fluid is known as viscoelastic parameter, denoted by k. Such polymers are employed as shock absorbers, to damp noises and confine vibrations, and discharge the energy absorbed as heat.

1.8.4 Deborah Number

It is a dimensionless quantity, proposed by Mark Reiner and named after the prophetess Deborah. It is utilized in rheology to describe the fluidity of substances under respective conditions. It is the ratio of the relaxation time taken by a substance to adjust as a result of deformation and applied stress, given as:

$$\beta_1 = \lambda_2 a. \tag{1.26}$$

Here λ_2 is the retardation time and a the strain rate.

1.9 Solution Approach

In this section, the solution methodology to solve the non-linear system of ODEs is presented.

1.9.1 Collocation Method-bvp4c

To determine the solution to the problem, perturbation expansion is adopted. The numerical outcomes for the equations obtained are computed by a finite-difference based technique-bvp4c built-in Matlab®. It is an effective and widely practiced numerical computational method for solving boundary value problems (BVP). This scheme works on the fundamental principles of calculus (infinitesimal differences) and utilizes the IIIa Lobatto formula, producing a class C^1 or continuously differentiable solutions (smoothness). Basically it is a residual-type scheme, in which the solution's residuality selects the mesh and controls the error count. The higher-ordered equations are converted into a system of first-order ODEs by importing a set of variables with corresponding boundary conditions, values for the constants involved, and an initial guess.

The working mechanism of this scheme is presented in the flow diagram below.

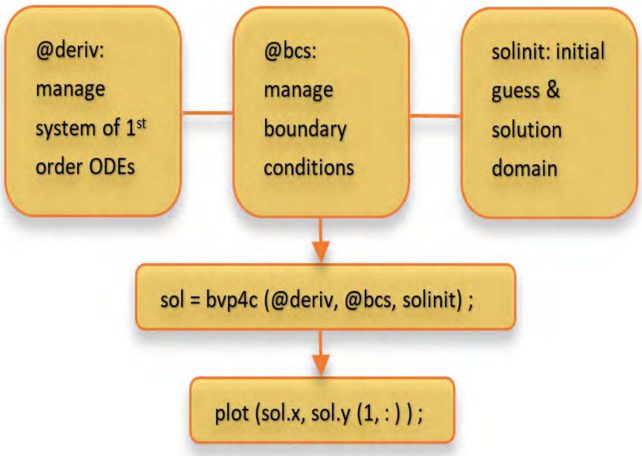

```
sol = bvp4c (@deriv, @bcs, solinit) ;
plot (sol.x, sol.y (1, : ) ) ;
```

Fig. 1 : Flow diagram of bvp4c technique.

1.10 Literature Review

Because of their intricate relation between deformation and stress rate, memory effect and rheological features, fluids with such characteristics and variable viscosity are categorized as non-Newtonian (polymeric liquids). They form an extensive range of products scilicet molten polymers, paints, thermoplastics, starch suspension, and so forth, that do not obey *Newton's viscous law*. Due to their promising applications in nearly every field and industry, their study is of eclectic interest for many engineers, mathematicians, and physicists. Before-mentioned fluids obey the *power-law model*, which explains that stress functions nonlinearly with the deformation rate. Since the classical theory of Navier-Stokes (NS) was unsuited to suggest the flow description of the before-mentioned fluids, therefore constitutive equations with the corresponding stress tensor were obtained to model the viscoelastic conduct of such fluids.

Amongst several models for non-Newtonian fluids, the center of discussion in this thesis are Walter's B liquid and Jeffrey fluid model. Walter [1] proposed the viscoelastic model, namely Walter's liquid model-B, which accurately incorporated the perplexing behavior of many industrial fluids and their elastic characteristics. The equations generated by the stress tensor are extremely non-linear in nature, whose solutions are computed by numerous distinct techniques.

Bariş [2] analyzed the impact of heat transport on the channel's wall for three-dimensional Walter's B flow model. The stagnation flow along with slip condition for Walter's B liquid was scrutinized by Labropulu *et al.* [3] past a rigid surface. Tonekaboni *et al.* [4] examined Walter's B flow for Blasius, stagnation region, and Sakiadis flows by using boundary layer approximation. Mdallal *et al.* [5] presented heat-mass transport analysis with their applications of fractional Walter's B fluid. Mahapatra and Sidui [6] reviewed the modified Homann flow for Walter's B liquid past a rigid plate. They computed numerical solutions for the problem and compared them with their asymptotic results. Jeffrey fluid model is a generalization of the classical Newton's viscous model. This model can determine the stress-relaxation and relaxation time (memory time scale) characteristic of polymeric liquids/physiological fluids. Khadrawi *et al.* [7] found semi-analytical solutions and studied velocity and shear-type driving forces for Couette flow, Poiseuille flow on parallel plates, and wind-driven flow on a finite domain, with the impact of Jeffrey fluid model. Akbar *et al.* [8] used Jeffery's flow model for the bloodstream with stenosis with a narrowed artery and found an approximate solution by perturbation. Khan *et al.* [9] studied the flow under constant applied stress caused by an oscillating and an accelerating plate.

Flow in the Stagnation-region (where the fluid flow is stationary) is another fascinating subject for fluid mechanics enthusiast. Since pressure is greatest when the velocity of a fluid is zero (*Bernoulli's equations*), wherefore, it is evident that pressure is highest in the stagnation zone, identified as the *stagnation pressure*. Due to the excessive pressure and heat transport rate at the stagnation-point, it is counted among the interesting problems and has many industrial uses as well. Hiemenz [10] in 1911 pioneered and obtained the solution for a planner stagnation region past a flat surface. He projected that from stagnation-point, the velocities at various positions are identical. Later on, in 1936, Homann [11] analyzed and determined the solution for the problem of axisymmetric flow. Howarth [12] in 1951 updated the solution presented by Hiemenz. While Darvey [13] in 1961 examined Howarth's equation and presented the saddle point solution. Garg [14] adopted a numerical approach to evaluate the heat transportation of a second-ordered fluid in the stagnation zone. Seshadri *et al.* [15] analyzed the unsteady viscoelastic flow in the stagnation-point and verified that free stream velocity significantly affects the results. Wang [16] on a shrinking/stretching sheet, studied the impression of non-alignment of stagnation flow. He demonstrated this concept by the example of a balloon. He concluded that the symmetry was disturbed and flow was obscured by non-alignment and shrinking/stretching of the sheet. Abbassi *et al.* [17] surveyed out the heat transport and computed solution for viscous stagnation flow by practicing potential theory. The formulation of Homann's problem for non-axisymmetric viscous flow was done by Weidman. [18]. Additionally, the Argawal and Homann flow in the stagnation region for the spiraling disk was investigated by Weidman [19]. The merging impacts of a transpired wall and plate stretchiness on Homann flow were addressed by Weidman and Ma [20]. They performed stability analysis and determined the dual and unique solutions. Mahapatra and Sidui [21] performed a thermal transport study for Homann flow near-stagnation zone. They found the presence of dual solutions, distinguished the uniqueness of solutions collectively with stability analysis.

The term *nanofluid* refers to the nanometer structured particles suspended in a base-fluid, where base-fluids are mostly composed of Dihydrogen oxide (H_2O), some intricate compounds of hydrocarbons, *i.e.*, $1,2$-Dihydroxyethane and crude oil (nano-lubricants). In the recent era, due to the extensive applications of nanofluids in applied science, automobiles, biomedicine, combustion of diesel, cooling of nuclear systems, electronics, and engines, energy conservation, industries, lubrication, nano-cryosurgery, refining of fuel, solar-cells, and welding, they have gained more attention. Due to the better stability and thermal conductivity of nanofluid, their utilization in engineering and industries are of exceptional significance to many researchers and scientists. They can be categorized as heat transfer nanofluids, bio-pharmaceutical nanofluids, extraction and environmental nanofluids, etc. Heat transfer analysis in a system inspects the production, exchange, conversion, and utilization of energy, by conduction/diffusion, radiation, advection, and convection mechanisms. Their applications comprise bio-MEMS, Doppler and Sympathetic cooling, fire alarm, magnetic refrigeration, smart-meter, thermal transmittance, thermostat, and so on. In 1995 Choi [22] proposed the term nanofluid for the very first time, since then, numerable studies have been supervised. Cheng [23] discussed nanofluid heat transfer technologies and the scope of their development in the future. For mathematical modeling of nanofluid transport, a two-phased model was demonstrated by Buongiorno [24], in which he depicted that the thermal conduction of nanofluids was boosted as a consequence to the participation of the Brownian motion and Ludwig–Soret effect (thermomigration). A single phased model for nanofluid flow was given by Tiwari and Das [25] in which they incorporated the impact of volume fraction. Wong's [26] work focused mainly on the present and future utilization of nanofluids. Fascinated by their work, many researches had been carried out since then regarding the utility of nanofluids, some of them are [27] & [28] . Sajid and Ali [29] presented positive and negative aspects related to the applications of nanofluids. They also collated and inspected different correlations employed for experiments in reviewed studies.

Researches regarding non-linear Rosseland radiation and magnetohydrodynamics (MHD) are applicable on various mechanisms, such as carbon dating, diagnosis and operation of diseases (PET scan), mining, smoke detectors, conversion of kinetic/thermal energy into electric energy (MHD generators), induction-conduction machines (MHD thrusters), marine and plasma propulsion engines (MHD propulsion), and nuclear weaponry, and so forth. Due to solar radiation, the average kinetic energy of a system is boosted, which enhances the chaotic motion of the particles, affecting the concentration of particles as well as the temperature of the system. Moreover, owing to the magnetic field, flow experience a resisting force (electromagnetic force) identified as the *Lorentz force*, which tapers rapidity of an electrically conducting fluid. However, heat conduction is enhanced by Joule heating phenomenon driven by MHD effect. Ahmed *et al.* [30] conducted an analytical study in which they examined the transference of heat through convection, including viscous and energy dissipation for a stretching sheet. Shehzad *et al.* [31] for a stretching surface presented Jeffrey's flow with heat generation and radiation. Farooq *et al.* [32] in their work investigated effect of MHD on viscoelastic fluid with non-linear radiation effects and concluded that concentration of nanoparticles decreases with an increment in Brownian diffusion. Raju *et al.* [33] gave solutions and analyzed Jeffrey fluid model with homogeneous-heterogeneous reaction past a stretching/shrinking surface. They deployed the shooting technique to obtain the outcomes and stated the range of the dual solutions for a particular extend of the parameters associated. Reddy *et al.* [34] considered the radiation effect on the Jeffrey fluid past an inclined vertical plate. They found the reducing relation of the radiation with the rate of heat transportation. Hussain *et al.* [35] analyzed the steady incompressible viscoelastic nanofluid with radiation. Besthapu *et al.* [36] for convective stretching surface, studied radiation and MHD influence in the stagnation zone of non-Newtonian nanofluid. Moreover, they deduced noteworthy impacts of the Casson fluid parameter on skin friction. Almakki *et* *al.* [37] presented a generalized representation for the stagnation-point of Jeffrey, Oldroyd-B, and Maxwell nanofluids flow. They analyzed the entropy production rate in laminar nanofluid flow and concluded that by increasing Deborah number entropy generation was enhanced.

Chapter 2 explores the non-axisymmetric Homann flow near the stagnation-zone of Walter's B nanofluid model along with magnetohydrodynamic (MHD) and non-linear Rosseland thermal radiation over a cylindrical disk. The impressions of thermo-diffusion and Brownian diffusion are analyzed by Buongiorno's model, with a time-independent free stream. The constitutive equations are determined and transformed into the dimensionless coupled ODEs via germane conversion functions. The ODEs are later numerically computed by altering the values of the pertinent parameters. Moreover, the numerical and asymptotic solutions for large values of shear-to-strain-rate ratio are computed and illustrated in graphs. The observations made are published in **"Applied Mathematics and Mechanics-English Edition, 41, (2020) 725-740".**

Chapter 3 includes the study of Jeffrey's nanofluid flow for non-axisymmetric Homann's flow in the stagnation-region with an electrically conducting flow over a cylindrical disk by Buongiorno's model. The outcomes of the solar radiation, thermo-migration, and Brownian diffusion on the concentration and thermal boundary layer are also scrutinized. By similarity transformation analysis, the conservation laws are turned into highly non-linear ordinary differential equations ODEs. A comparative study among the numerical and asymptotic solutions for the parameters of displacement thicknesses and wall-shear stress is executed. The consequence of Jeffrey's material parameters and magnetic field on displacement thickness is explained. The finite difference method is utilized for computations of the flow, energy, displacement thickness, skin friction force, and concentration distribution.

Chapter 2

Non-Axisymmetric Homann Stagnation-point Flow of Walter's B Nanofluid over a Cylindrical Disk

In this chapter, the study of non-axisymmetric Homann stagnation-point flow of Walter's B nanofluid along with magnetohydrodynamic (MHD) and non-linear Rosseland thermal radiation over a cylindrical disk in the existence of the time-independent free stream is considered. Moreover, the notable impacts of thermophoresis and Brownian motion are analyzed by Buongiorno's model. The momentum, energy, and concentration equations are converted into the dimensionless coupled ordinary differential equations via similarity transformations, which are later numerically solved by altering the values of the pertinent parameters. The numerical and large valued shear-to-strain ratio $\gamma = \frac{b}{a}$ asymptotic solutions for the parameters of displacement thicknesses and wall-shear stress are computed by perturbative expansion and analyzed. Furthermore, the technique bvp4c in Matlab® is deployed as an efficient method to analyze the calculations for the non-dimensional velocities, temperature, displacement thickness, and concentration profiles. It is observed that the two-dimensional displacement thickness parameters are reduced due to the viscoelasticity and magnetic field effects and when shear-to-strain-rate ratio approaches infinity, displacement thickness parameters along x-axis is closer to its asymptotic value, but displacement thickness parameters along y-axis and three-dimensional displacement thickness parameter show the opposite trend. The outcomes of viscoelasticity and magnetic field on the skin friction are also determined. It is concluded that coefficient of skin-friction along x-direction reaches its asymptotic behavior when the shear-to-strain-rate ratio approaches infinity; however, the coefficient of skin friction along y-direction shows different results.

2.1 Problem Formulation

2.1.1 Coordinates Transformation

The 3D viscoelastic stagnation-point flow over a cylindrical disk along is considered. By superposing $r\sin 2\vartheta$ and $r\cos 2\vartheta$ onto Homann's external potential flow, the potential flow field in cylindrical coordinates system (r, ϑ, z) with $(\breve{u}_r, \breve{u}_\vartheta, \breve{u}_z)$ in terms of strain rate a and shear rate b, by following Weidman [18] is given as:

$$\breve{u}_r\left(r, \vartheta\right) = ra + rb\sin 2\vartheta,\ \ \breve{u}_\vartheta\left(r, \vartheta\right) = rb\cos 2\vartheta,\ \ \breve{u}_z\left(z\right) = -2az. \tag{2.1}$$

Note that Eq. (2.1) satisfies the continuity equation.

To note the impact and signify the importance of the periodic terms in the potential flow in cylindrical coordinates (r, ϑ, z) at nodal stagnation-zone for viscoelastic fluid, we have transformed the potential function in Cartesian coordinates (x, y, z) with velocity $(\breve{u}, \breve{v}, \breve{w})$, which is computed by a rotation matrix given as:

$$\breve{u}\left(x, y\right) = ax + by,\ \ \breve{v}\left(x, y\right) = bx + ay,\ \ \breve{w}\left(z\right) = -2az. \tag{2.2}$$

To find components along the principal axes (x', y', z'), we apply basic concepts of matrix theory from linear algebra. Firstly, we write the horizontal velocities $\breve{u}$ and $\breve{v}$ in matrix representation as:

$$\begin{bmatrix} \breve{u} \\ \breve{v} \end{bmatrix} = \breve{A}\begin{bmatrix} x \\ y \end{bmatrix} \equiv \begin{bmatrix} a & b \\ b & a \end{bmatrix}\begin{bmatrix} x \\ y \end{bmatrix}. \tag{2.3}$$

Then, Eq. (2.3) is diagonalized along the principal axes with the velocities $(\breve{u}', \breve{v}')$,determined as:

$$\begin{bmatrix} \breve{u}' \\ \breve{v}' \end{bmatrix} = \Lambda \begin{bmatrix} x' \\ y' \end{bmatrix} \equiv \begin{bmatrix} \lambda & 0 \\ 0 & \lambda \end{bmatrix} \begin{bmatrix} x' \\ y' \end{bmatrix}. \tag{2.4}$$

By practicing *characteristics equation* $\det\left[\breve{A} - \lambda I\right] = 0$, we determined the eigenvalues $\lambda = a \pm b$. The exterior potential flow is obtained by rotation along (x', y', z').

$$\breve{u}'(x', y') = x'(a+b)\,,\ \breve{v}'(x', y') = y'(a-b)\,,\ \breve{w}'(z') = -2az'. \tag{2.5}$$

The velocity field along the principal axes is $\mathbf{V} = [\breve{u}', \breve{v}', \breve{w}']$. By considering the flow along principal axis, we can let go of the prime symbol in Eq. (2.5) , as it does not affect our problem. This approach is also adopted to transform the coordinates in Chapter 3.

2.1.2 Mathematical Modeling

We thoroughly explored the results of non-linear radiation and MHD for steady, incompressible Walter's B nanofluid flow. The center of our attention here is to inspect the outcomes of effects considered for a viscoelastic nanofluid flow near the stagnation-zone by adopting the Buongiorno model. We have induced the magnetic field $\mathbf{B}$ along the z-direction, as $[0, 0, B_0]$, where B_0 is the magnetic field intensity. Here at cylinder's wall the fluid temperature is $\breve{T}(x, y, z) = \breve{T}_w$ with concentration as $\breve{C}(x, y, z) = \breve{C}_w$. In Fig. 1, the flow diagram is illustrated. By adding $r \sin 2\vartheta$ and $r \cos 2\vartheta$ onto Homann's external potential flow, we determined it in cylindrical coordinates system (r, ϑ, z) and modified it into Cartesian coordinates (x, y, z), as presented in § 2.1.1.

The potential flow in Cartesian coordinates is:

$$\mathbf{V} = [\breve{u}, \breve{v}, \breve{w}] = [x(a+b), y(a-b), -2az]. \tag{2.6}$$

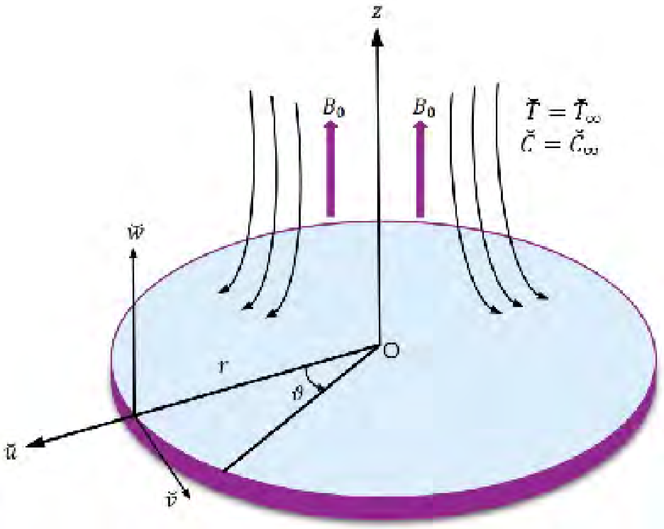

Fig. 2.1 : Flow mechanism.

The conservation laws for the problem are given in § 1.6 of Chapter 1. The stress tensor for Walter's B-liquid with the strain-rate tensor e_{ab} is written in § 1.7.1. By using the components of stress tensor from § 1.7.1 and BL approximation stated in § 1.5.1 of Chapter 1, the above conservation equations for incompressible steady flow are reduced as:

$$\frac{\partial \breve{u}}{\partial x} + \frac{\partial \breve{v}}{\partial y} + \frac{\partial \breve{w}}{\partial z} = 0, \tag{2.7}$$

$$\begin{aligned} \breve{u}\frac{\partial \breve{u}}{\partial x} + \breve{v}\frac{\partial \breve{u}}{\partial y} + \breve{w}\frac{\partial \breve{u}}{\partial z} &= -\frac{1}{\rho}\frac{\partial p}{\partial x} + \nu\frac{\partial^2 \breve{u}}{\partial z^2} - \frac{\sigma B_0^2 \breve{u}}{\rho} \\ -\frac{k_0}{\rho}\left[\breve{u}\frac{\partial^3 \breve{u}}{\partial x \partial z^2} - 2\frac{\partial^2 \breve{u}}{\partial x \partial z}\frac{\partial \tilde{u}}{\partial z} - \frac{\partial^2 \breve{u}}{\partial z^2}\frac{\partial \breve{u}}{\partial x} - 2\frac{\partial^2 \breve{u}}{\partial z^2}\frac{\partial \breve{w}}{\partial z} + \breve{w}\frac{\partial^3 \breve{u}}{\partial z^3} - \frac{\partial^2 \breve{w}}{\partial z^2}\frac{\partial \breve{u}}{\partial z}\right], \end{aligned} \tag{2.8}$$

$$\begin{aligned} \breve{u}\frac{\partial \breve{v}}{\partial x} + \breve{v}\frac{\partial \tilde{v}}{\partial y} + \breve{w}\frac{\partial \breve{v}}{\partial z} &= -\frac{1}{\rho}\frac{\partial p}{\partial y} + \nu\frac{\partial^2 \breve{v}}{\partial z^2} - \frac{\sigma B_0^2 \breve{v}}{\rho} \\ -\frac{k_0}{\rho}\left[\breve{v}\frac{\partial^3 \breve{v}}{\partial y \partial z^2} - 2\frac{\partial^2 \breve{v}}{\partial y \partial z}\frac{\partial \breve{v}}{\partial z} - \frac{\partial^2 \breve{v}}{\partial z^2}\frac{\partial \breve{v}}{\partial y} - 2\frac{\partial^2 \breve{v}}{\partial z^2}\frac{\partial \breve{w}}{\partial z} + \breve{w}\frac{\partial^3 \breve{v}}{\partial z^3} - \frac{\partial^2 \breve{w}}{\partial z^2}\frac{\partial \breve{v}}{\partial z}\right], \end{aligned} \tag{2.9}$$

$$\breve{u}\frac{\partial \breve{T}}{\partial x} + \breve{v}\frac{\partial \breve{T}}{\partial y} + \breve{w}\frac{\partial \breve{T}}{\partial z} = \alpha_{nf}\frac{\partial^2 \breve{T}}{\partial z^2} - \frac{1}{(\rho c)_p}\frac{\partial q_T}{\partial z} + \frac{(\rho c)_{nf}}{(\rho c)_p}\left[D_B\frac{\partial \breve{T}}{\partial z}\frac{\partial \breve{C}}{\partial z} + \frac{D_T}{\breve{T}_\infty}\left(\frac{\partial \breve{T}}{\partial z}\right)^2\right], \tag{2.10}$$

$$\breve{u}\frac{\partial \breve{C}}{\partial x}+\breve{v}\frac{\partial \breve{C}}{\partial y}+\breve{w}\frac{\partial \breve{C}}{\partial z}=D_B\frac{\partial^2 \breve{C}}{\partial z^2}+\frac{D_T}{\breve{T}_\infty}\left(\frac{\partial^2 \breve{T}}{\partial z^2}\right). \tag{2.11}$$

By adopting Rosseland/diffusion approximation, q_T the radiative flux [38] is interpreted as:

$$q_T=-\frac{4\sigma^*}{3k^*}\frac{\partial \breve{T}^4}{\partial z}=-\frac{16\sigma^*\breve{T}^3}{3k^*}\frac{\partial \breve{T}}{\partial z}, \tag{2.12}$$

where σ^* and k^* denote the Stefan's constant and the mean absorption coefficient, respectively. Putting Eq. (2.12) in Eq. (2.10), we have

$$\breve{u}\frac{\partial \breve{T}}{\partial x}+\breve{v}\frac{\partial \breve{T}}{\partial y}+\breve{w}\frac{\partial \breve{T}}{\partial z}=\alpha_{nf}\frac{\partial^2 \breve{T}}{\partial z^2}+\frac{\partial}{\partial z}\left(\frac{16\sigma^*\breve{T}^3}{3k^*(\rho c)_p}\frac{\partial \breve{T}}{\partial z}\right)+\frac{(\rho c)_{nf}}{(\rho c)_p}\left[D_B\frac{\partial \breve{T}}{\partial z}\frac{\partial \breve{C}}{\partial z}+\frac{D_T}{\breve{T}_\infty}\left(\frac{\partial \breve{T}}{\partial z}\right)^2\right]. \tag{2.13}$$

In the Eqs. (2.8) and (2.9) , the terms of pressure gradient at free-stream with velocities $\left(\breve{U}_\infty,\breve{V}_\infty\right)$ are given as:

$$\left.\begin{array}{l}\breve{U}_\infty\frac{\sigma B_0^2}{\rho}+\breve{U}_\infty\frac{\partial \breve{U}_\infty}{\partial x}=-\frac{1}{\rho}\frac{\partial p}{\partial x},\\ \breve{V}_\infty\frac{\sigma B_0^2}{\rho}+\breve{V}_\infty\frac{\partial \breve{V}_\infty}{\partial y}=-\frac{1}{\rho}\frac{\partial p}{\partial y}.\end{array}\right\} \tag{2.14}$$

2.1.3 Boundary Conditions

Since the problem is modeled with no-slip condition and at the free stream, the boundary conditions become:

$$\breve{u}=0,\ \breve{v}=0,\ \breve{w}=0,\ \breve{T}=\breve{T}_w,\ C=C_w \quad \text{at } z=0, \tag{2.15}$$

$$\breve{u}\to x(a+b),\ \breve{v}\to y(a-b),\ \breve{w}\to -2az,\ \breve{T}\to \breve{T}_\infty,\ C\to C_\infty \text{ as } z\to\infty. \tag{2.16}$$

2.1.4 Similarity Transformations

Introducing the subsequent conversions to transform the Eqs. (2.11) – (2.14).

$$\begin{aligned}&\breve{u}\,(x,y)=x\,(a+b)\,\breve{f}'(\eta),\quad \breve{v}\,(x,y)=y\,(a-b)\,\breve{g}'(\eta),\\ &\breve{w}\,(z)=-\sqrt{\frac{\nu}{a}}\left[(a+b)\,\breve{f}(\eta)+(a-b)\,\breve{g}(\eta)\right],\end{aligned} \tag{2.17}$$

$$\theta\,(\eta)=\frac{\breve{T}-\breve{T}_\infty}{\breve{T}_w-\breve{T}_\infty},\quad \phi\,(\eta)=\frac{\breve{C}-\breve{C}_\infty}{\breve{C}_w-\breve{C}_\infty},\ \text{where } \eta=\sqrt{\frac{a}{\nu}}z, \tag{2.18}$$

where ν the kinematic viscosity, $\theta\left(\eta\right)$ and $\phi\left(\eta\right)$ denote the fluid temperature and concentration, respectively. Note that, Eq. (2.17) satisfies the continuity equation. Utilizing the Eqs. (2.17) and (2.18), we can write the momentum, energy, and concentration equations as:

$$\begin{aligned} &\breve{f}''' - \left(1+\gamma\right)\left[\breve{f}'^{2} - \breve{f}\breve{f}'' - 1 + k\left(2\breve{f}'\breve{f}''' - \breve{f}''^{2} - \breve{f}\breve{f}^{iv}\right)\right] \\ &+ \left(1-\gamma\right)\left[\breve{g}\breve{f}'' + k\left(\breve{g}\breve{f}^{iv} - \breve{f}''\breve{g}'' - 2\breve{f}'''\breve{g}'\right)\right] - M^{2}\left(\breve{f}' - 1\right) = 0, \end{aligned} \tag{2.19}$$

$$\begin{aligned} &\breve{g}''' - \left(1-\gamma\right)\left[\breve{g}'^{2} - \breve{g}\breve{g}'' - 1 + k\left(2\breve{g}'\breve{g}''' - \breve{g}''^{2} - \breve{g}\breve{g}^{iv}\right)\right] \\ &+ \left(1+\gamma\right)\left[\breve{f}\breve{g}'' + k\left(\breve{f}\breve{g}^{iv} - \breve{g}''\breve{f}'' - 2\breve{g}'''\breve{f}'\right)\right] - M^{2}\left(\breve{g}' - 1\right) = 0, \end{aligned} \tag{2.20}$$

$$\begin{aligned} &\theta'' + \mathrm{Pr}\left[\breve{f}\left(1+\gamma\right)\theta' + \breve{g}\left(1-\gamma\right)\theta' + N_t\left(\theta\right)'^{2} + N_b\left(\theta'\phi'\right)\right] \\ &+ R_d\left[3\theta'^{2}\left(1+\theta\left(\theta_w - 1\right)\right)^{2}\left(\theta_w - 1\right) + \theta''\left(1+\theta\left(\theta_w - 1\right)\right)^{3}\right] = 0, \end{aligned} \tag{2.21}$$

$$\phi'' + Sc\left[\breve{f}\left(1+\gamma\right) + \breve{g}\left(1-\gamma\right)\right]\phi' + \frac{N_t}{N_b}\theta'' = 0, \tag{2.22}$$

where the dimensionless parameters $M,\ k,\ Sc,\ R_d,\ Pr,\ N_t,\ \theta_w$, and N_b represent the magnetic parameter, the viscoelastic parameter, the Schmidt number, the radiation coefficient, the Prandtl number, the thermophoresis, the temperature-ratio, and the Brownian diffusion parameter, respectively. The values of these dimensionless parameters are

$$\begin{aligned} M &= \sqrt{\frac{\sigma}{a\rho}}B_0,\ k = \frac{k_0 a}{\rho\nu},\ Sc = \frac{\nu}{D_B},\ Pr = \frac{\nu}{\alpha_{nf}}, \\ R_d &= \frac{16\sigma^{*}\breve{T}_{\infty}^{3}}{3k^{*}k_{nf}}, N_t = \frac{D_T\left(\breve{T}_w - \breve{T}_{\infty}\right)\left(\rho c\right)_{nf}}{\breve{T}_{\infty}\nu\left(\rho c\right)_p}, \\ \theta_w &= \frac{\breve{T}_w}{\breve{T}_{\infty}},\ N_b = \frac{D_B\left(\breve{C}_w - \breve{C}_{\infty}\right)\left(\rho c\right)_{nf}}{\nu\left(\rho c\right)_p}. \end{aligned} \tag{2.23}$$

Using Eqs. (2.17) & (2.18), we get the boundary conditions.

$$\breve{f}\left(0\right) = 0,\ \breve{f}'\left(0\right) = 0,\ \breve{g}\left(0\right) = 0,\ \breve{g}'\left(0\right) = 0,\ \theta\left(0\right) = 1,\ \phi\left(0\right) = 1, \tag{2.24}$$

$$\breve{f}'(\infty) = 1,\ \breve{g}'(\infty) = 1,\ \theta(\infty) = 0,\ \phi(\infty) = 0. \tag{2.25}$$

2.1.5 Shear Stress

Wall shear-stress $\boldsymbol{\tau}$ calculated is identical to viscous fluid case (see Weidman [18]).

$$\boldsymbol{\tau} = \left[(\tau_{13})\,\mathbf{i} + (\tau_{23})\,\mathbf{j} \right|_{z=0}, \tag{2.26}$$

where

$$\begin{aligned} \left[\tau_{13}\right|_{z=0} &= x\breve{f}''(0)\,\frac{\mu a^{\frac{3}{2}}(1+\gamma)}{\sqrt{\nu}}, && (2.27)\\ \left[\tau_{23}\right|_{z=0} &= y\breve{g}''(0)\,\frac{\mu a^{\frac{3}{2}}(1-\gamma)}{\sqrt{\nu}}. && (2.28)\end{aligned}$$

Eq. (2.26) becomes:

$$\boldsymbol{\tau} = \left(\frac{\mu a^{\frac{3}{2}}(1+\gamma)}{\sqrt{\nu}}x\breve{f}''(0)\right)\mathbf{i} + \left(\frac{\mu a^{\frac{3}{2}}(1-\gamma)}{\sqrt{\nu}}y\breve{g}''(0)\right)\mathbf{j}. \tag{2.29}$$

2.1.6 Displacement Thicknesses

After calculating the solution, we move forward to determine the 2D boundary layer displacement thicknesses δ_x and δ_y. Furthermore, the 3D boundary-layer displacement thickness δ_1 is calculated (see Davey [13] and Lighthill [40])

$$\sqrt{\frac{a}{\nu}}\delta_x = \int_0^\infty \left[1 - \frac{\breve{u}}{\breve{U}_\infty}\right] d\eta = \int_0^\infty \left[1 - \breve{f}'(\eta)\right] d\eta, \tag{2.30}$$

$$\sqrt{\frac{a}{\nu}}\delta_y = \int_0^\infty \left[1 - \frac{\breve{v}}{\breve{V}_\infty}\right] d\eta = \int_0^\infty \left[1 - \breve{g}'(\eta)\right] d\eta, \tag{2.31}$$

and

$$\delta_1 = \frac{(1+\gamma)\,\alpha + (1-\gamma)\,\beta}{2}. \tag{2.32}$$

It is noted that as γ approaches infinity, δ_x and δ_y reaches zero, meanwhile $\delta_1 \to -\infty$. Further discussion of these parameters is presented in § 2.3.7.

2.2 Numerical Solutions

To procure the solution to the problem, perturbation expansion is adopted. The numerical outcomes for the equations determined are computed by a finite-difference based technique-bvp4c in Matlab®. The high-ordered equations are modified into first-order ODEs by a set of variables with corresponding boundary conditions, values for the constants associated, and an initial guess as discussed in § 1.9 of Chapter 1.

2.2.1 Regular Perturbation Expansion

The aim of this section is to calculate the numerical results for the flow field. To get the solutions of the problem, perturbation expansion is employed. Since, in Eqs. (2.19) and (2.20) the viscoelastic parameter is non-zero, *i.e.*, $k \neq 0$, they involve the forth-order differential equations and boundary conditions are not sufficient to compute the solution. Thus, we adopt the approach used by Beard [39], by taking the viscoelastic parameter very small, *i.e.*, $k \ll 1$ to calculate the solution as:

$$\breve{f}(\eta) = \breve{f}_0(\eta) + k\breve{f}_1(\eta) + k^2\breve{f}_2(\eta) + \cdots, \tag{2.33}$$

$$\breve{g}(\eta) = \breve{g}_0(\eta) + k\breve{g}_1(\eta) + k^2\breve{g}_2(\eta) + \cdots. \tag{2.34}$$

Putting Eqs. (2.33) and (2.34) in Eqs. (2.19) and (2.20) and equating the coefficients of k^0 and k^1:

$$\breve{f}_0''' - (1+\gamma)\left(\breve{f}_0'^2 - \breve{f}_0\breve{f}_0'' - 1\right) + (1-\gamma)\,\breve{g}_0\breve{f}_0'' - M^2\left(\breve{f}_0' - 1\right) = 0, \tag{2.35}$$

$$\breve{g}_0''' - (1-\gamma)\left(\breve{g}_0'^2 - \breve{g}_0\breve{g}_0'' - 1\right) + (1+\gamma)\,\breve{f}_0\breve{g}_0'' - M^2\left(\breve{g}_0' - 1\right) = 0, \tag{2.36}$$

$$\begin{aligned}&\breve{f}_1''' - (1+\gamma)\left(2\breve{f}_0'\breve{f}_1' - \breve{f}_0\breve{f}_1'' - \breve{f}_1\breve{f}_0'' + 2\breve{f}_0'\breve{f}_0''' - \breve{f}_0''^2 - \breve{f}_0\breve{f}_0''''\right)\\ &+ (1-\gamma)\left(\breve{g}_0\tilde{f}_1'' + \breve{g}_0\tilde{f}_0'''' + \breve{g}_1\tilde{f}_0'' - \tilde{f}_0''\breve{g}_0'' - 2\tilde{f}_0'''\breve{g}_0'\right) - M^2\tilde{f}_1' = 0,\end{aligned} \tag{2.37}$$

$$\begin{aligned}&\breve{g}_1''' - (1-\gamma)\left(2\breve{g}_0'\breve{g}_1' - \breve{g}_0\breve{g}_1'' - \breve{g}_1\breve{g}_0'' + 2\breve{g}_0'\breve{g}_0''' - \breve{g}_0''^2 - \breve{g}_0\breve{g}_0''''\right)\\ &+ (1+\gamma)\left(\breve{g}_0\breve{f}_1'' + \breve{f}_0\breve{g}_1'' + \breve{f}_0\breve{g}_0'''' + \breve{f}_1\breve{g}_0'' - \breve{g}_0''\breve{f}_0'' - 2\breve{g}_0'''\breve{f}_0'\right) - M^2\breve{g}_1' = 0.\end{aligned} \tag{2.38}$$

with boundary conditions

$$\breve{f}_0\left(0\right)=0,\ \breve{f}_0'\left(0\right)=0,\ \breve{f}_0'\left(\infty\right)=1,\ \breve{f}_1\left(0\right)=0,\ \breve{f}_1'\left(0\right)=0,\ \breve{f}_1'\left(\infty\right)=0, \tag{2.39}$$

$$\breve{g}_0\left(0\right)=0,\ \breve{g}_0'\left(0\right)=0,\ \breve{g}_0'\left(\infty\right)=1,\ \breve{g}_1\left(0\right)=0,\ \breve{g}_1'\left(0\right)=0,\ \breve{g}_1'\left(\infty\right)=0. \tag{2.40}$$

Using Eqs. (2.33) and (2.34) in Eqs. (2.30) and (2.31) we get perturbed equations for 2D displacement thicknesses as:

$$\sqrt{\frac{a}{\nu}}\delta_x=\int\limits_0^\infty\left[1-\breve{f}_0'\left(\eta\right)-k\breve{f}_1'\left(\eta\right)\right]d\eta\equiv\alpha, \tag{2.41}$$

$$\sqrt{\frac{a}{\nu}}\delta_y=\int\limits_0^\infty\left[1-\breve{g}_0'\left(\eta\right)-k\breve{g}_1'\left(\eta\right)\right]d\eta\equiv\beta, \tag{2.42}$$

where α and β are displacement thickness parameters in 2D.

2.2.2 Asymptotic for $\gamma \gg 1$

By changing variables, the asymptotic conduct of solution is calculated for large-γ as:

$$\breve{f}\left(\eta\right)=\epsilon\breve{F}\left(\xi\right),\ \text{and}\ \breve{g}\left(\eta\right)=\epsilon\breve{G}\left(\xi\right), \tag{2.43}$$

with

$$\xi=\eta\epsilon^{-1},\ k=\epsilon^3,\ \text{and}\ \epsilon=\frac{1}{\sqrt{\gamma}}\ll 1. \tag{2.44}$$

On the account of above transformations, Eqs. (2.19) and (2.20) are transformed into

$$\begin{aligned}\breve{F}'''-\left(\epsilon^2+1\right)\left[\breve{F}'^2-\breve{F}\breve{F}''-1+\epsilon\left(2\breve{F}'\breve{F}'''-\breve{F}''^2-\breve{F}\breve{F}^{iv}\right)\right]\\+\left(\epsilon^2-1\right)\left[\breve{G}\breve{F}''+\epsilon\left(\breve{G}\breve{F}^{iv}-\breve{F}''\breve{G}''-2\breve{F}'''\breve{G}'\right)\right]-M^2\left(\breve{F}'-1\right)=0,\end{aligned} \tag{2.45}$$

$$\begin{aligned}\breve{G}'''-\left(\epsilon^2-1\right)\left[\breve{G}'^2-\breve{G}\breve{G}''-1+\epsilon\left(2\breve{G}'\breve{G}'''-\breve{G}''^2-\breve{G}\breve{G}^{iv}\right)\right]\\+\left(\epsilon^2+1\right)\left[\breve{F}\breve{G}''+\epsilon\left(\breve{F}\breve{G}^{iv}-\breve{G}''\breve{F}''-2\breve{G}'''\breve{F}'\right)\right]-M^2\left(\breve{G}'-1\right)=0.\end{aligned} \tag{2.46}$$

By regular perturbation expansion, we can write

$$\breve{F}\left(\xi\right)=\breve{F}_0\left(\xi\right)+\epsilon\breve{F}_1\left(\xi\right)+\epsilon^2\breve{F}_2\left(\xi\right)+\cdots, \tag{2.47}$$

$$\breve{G}\left(\xi\right)=\breve{G}_0\left(\xi\right)+\epsilon\breve{G}_1\left(\xi\right)+\epsilon^2\breve{G}_2\left(\xi\right)+\cdots. \tag{2.48}$$

Utilizing Eqs. (2.47) and (2.48) , the lowest and first order systems are written as:

$$\breve{F}_0'''-\breve{F}_0'^2+\breve{F}_0\breve{F}_0''+1-\breve{G}_0\breve{F}_0''=0, \tag{2.49}$$

$$\breve{G}_0'''+\breve{G}_0'^2-\breve{G}_0\breve{G}_0''-1+\breve{F}_0\breve{G}_0''=0, \tag{2.50}$$

$$\begin{aligned} &\breve{F}_1'''-2\breve{F}_0'\breve{F}_1'+\breve{F}_0\breve{F}_1''+\breve{F}_1\breve{F}_0''-2\breve{F}_0'\breve{F}_0'''+\breve{F}_0'' \\ &+\breve{F}_0\breve{F}_0^{iv}-\breve{G}_0\breve{F}_1''-\breve{G}_0\breve{F}_0^{iv}-\breve{G}_1\breve{F}_0''+\breve{F}_0''\breve{G}_0''+2\breve{F}_0'''\breve{G}_0'=0, \end{aligned} \tag{2.51}$$

$$\begin{aligned} &\breve{G}_1'''+2\breve{G}_0'\breve{G}_1'-\breve{G}_0\breve{G}_1''-\breve{G}_1\breve{G}_0''+2\breve{G}_0'\breve{G}_0'''-\tilde{G}_0'' \\ &-\breve{G}_0\breve{G}_0^{iv}+\breve{F}_0\breve{G}_1''+\breve{F}_0\breve{G}_0^{iv}+\breve{F}_1\breve{G}_0''-\breve{F}_0''\breve{G}_0''-2\breve{G}_0'''\breve{F}_0'=0. \end{aligned} \tag{2.52}$$

With boundary conditions:

$$\breve{F}_0\left(0\right)=0,\ \breve{F}_0'\left(0\right)=0,\ \breve{F}_0'\left(\infty\right)=1,\ \breve{F}_1\left(0\right)=0,\ \breve{F}_1'\left(0\right)=0,\ \breve{F}_1'\left(\infty\right)=0, \tag{2.53}$$

$$\breve{G}_0\left(0\right)=0,\ \breve{G}_0'\left(0\right)=0,\ \breve{G}_0'\left(\infty\right)=1,\ \breve{G}_1\left(0\right)=0,\ \breve{G}_1'\left(0\right)=0,\ \breve{G}_1'\left(\infty\right)=0. \tag{2.54}$$

Large-γ Shear Stress

Using Eqs. (2.43) and (2.44) the large-γ skin friction coefficients with the impression of magnetic field are stated as:

$$\breve{f}''\left(0\right)\sim\sqrt{\gamma}\left[\breve{F}_0''\left(0\right)+k\gamma\breve{F}_1''\left(0\right)\right], \tag{2.55}$$

$$\breve{g}''\left(0\right)\sim\sqrt{\gamma}\left[\breve{G}_0''\left(0\right)+k\gamma\breve{G}_1''\left(0\right)\right]. \tag{2.56}$$

Large-γ Displacement Thicknesses

By utilizing the asymptotic analysis, we can get a comparison between numerical and asymptotic solutions for displacement thickness parameters. Assume $\alpha = \epsilon\alpha^{*}$and $\beta = \epsilon\beta^{*}$, we have

$$\alpha^{*} = \int_{0}^{\infty} \left[1 - \breve{F}_0'(\xi)\right] d\xi - \epsilon \int_{0}^{\infty} \breve{F}_1'(\xi)\, d\xi = \alpha_0^{*} + \epsilon\alpha_1^{*}, \tag{2.57}$$

$$\beta^{*} = \int_{0}^{\infty} \left[1 - \breve{G}_0'(\xi)\right] d\xi - \epsilon \int_{0}^{\infty} \breve{G}_1'(\xi)\, d\xi = \beta_0^{*} + \epsilon\beta_1^{*}. \tag{2.58}$$

The large-γ with displacement thicknesses are given as

$$\alpha \sim \frac{\alpha^{*}}{\sqrt{\gamma}} \text{ and } \beta \sim \frac{\beta^{*}}{\sqrt{\gamma}}, \tag{2.59}$$

and

$$\delta^{*} \sim \frac{(1+\gamma)\,\alpha^{*} + (1-\gamma)\,\beta^{*}}{2\sqrt{\gamma}}. \tag{2.60}$$

2.2.3 Results Authentication

This section compares the outcomes of our study with the ones in literature. It can be clearly seen that Eqs. (2.19) and (2.20) are reflexive symmetry, *i.e.*,

$$\breve{f}(\eta, -\gamma) = \breve{g}(\eta, \gamma), \text{ and } \breve{g}(\eta, -\gamma) = \breve{f}(\eta, \gamma). \tag{2.61}$$

Note that, when $\gamma = M = 0$ in Eqs. (2.19) and (2.20), we can recover the axisymmetric Homann [11] flow equation, *i.e.*, $\breve{f}(\eta) = \breve{g}(\eta)$. Also, for $\gamma = 1$ and $M = 0$ in Eqs. (2.19) and (2.20), we can recover Hiemenz [10] equation. Moreover, for $M = 0$ in Eqs. (2.19) and (2.20) and no heat transport examination we can get Mahapatra and Sidui's [6] case. Also, using $k = 0$ and $M = 0$ in Eqs. (2.19) and (2.20), Weidman's [18] work is recovered. We can also get values of 2D displacement thickness parameters α and β for zeroth order as $\alpha_0^{*} = 0.610$, $\beta_0^{*} = 3.4384$ and first order as $\alpha_1^{*} = -0.9984$, $\beta_1^{*} = -3.9349$. The numerical values for asymptotic outcomes are compared with Refs. [6] and [18] in Table 1. These values are in excellent agreement with Davey [13].

Table 2.1 : Asymptotic behavior of Shear Stress parameters.

	Ref. [6]	**Ref.** [18]	**Present**
	$M=0$	$M=k=0$	$M=0$
$\breve{F}_0''(0)$	1.2729	1.2729	1.2729
$\breve{G}_0''(0)$	-0.8112	-0.8112	-0.8112
$\breve{F}_1''(0)$	1.2805		1.2805
$\breve{G}_1''(0)$	-0.4435		-0.4435

2.3 Graphical Discussion

The case of Walter's B nanofluid flow for modified Homann flow in the stagnation region is examined in this article. We applied a finite difference based method, bvp4c in Matlab® to compute the numerical outcomes. This section aims to address the numerical outcomes attained related to the flow along x- and y-directions $\breve{f}'(\eta)$ and $\breve{g}'(\eta)$, respectively, the 2D and 3D displacement thicknesses δ_x, δ_y and δ_1, respectively, fluid temperature $\theta(\eta)$ and its concentration $\phi(\eta)$ field for the involved parameters, *i.e.,* the magnetic parameter M, the viscoelastic parameter k, the Prandtl number Pr, the temperature-ratio θ_w, the thermophoresis N_t, the Schmidt number Sc, radiation parameter R_d, and the Brownian motion parameter N_b.

2.3.1 Impression of the Viscoelastic Parameter

The property of substances that experiences viscous and elastic qualities during deformation is described as viscoelasticity. Such polymers are employed as shock absorbers, to damp noises, confine vibrations, and discharge the energy absorbed as heat. Figs. 2.2(a) and 2.2(b) demonstrate the influence of viscoelasticity k on the flow. In Fig. 2.2(a) the velocity component along x-direction $\breve{f}'(\eta)$ is varied by increasing the values of k. It is perceived that due to viscoelasticity the flow along the x-axis is enhanced for a fixed value of $\gamma = 2$ and $M = 0.25$. Fig. 2.2(b) displays the behavior of velocity component along y-direction $\breve{g}'(\eta)$ with η for $\gamma = 2.505, 2.5183, 2.5994$ and $k = 0.0, 0.01, 0.07$, respectively. It is seen that reverse flow is exhibited towards the stagnation-point. However, the flow along the y-direction faced resistance and is reduced by increasing γ from 4 to 6 with $k = 0.07$, but after that opposite behavior is depicted. Figs. 2.2(c) displays that energy is discharged which results in the reduction in thermal field. Fig. 2.2$\,(d)$ shows that the mass transport phenomena is lessened. Figs. 2.2$\,(e)$ and 2.2$\,(f)$ depict the impact of γ on thermal and mass transport. It is noted that both of these fields are reduced by enhancing γ.

2.3.2 Impression of the Magnetic Field

Figs. 2.3$\,(a)$ − 2.3(d) highlight the contribution of magnetic field parameter M on the fluid flow $\breve{f}'(\eta)$ and $\breve{g}'(\eta)$, fluid temperature $\theta(\eta)$ and concentration $\phi(\eta)$ fields. It is noted that by enhancing magnetic field parameter M, the flow behavior lessened; however, the thermal conductivity and concentration profile are elevated. This is because the magnetic field generated a resistance force against the flow, known as Lorentz or electromagnetic force. This opposing force dissuades the significance of velocity profile, which as a result eventually decayed. In contrast, the thermal and concentration fields are raised significantly. This behavior magnified heat transport, and consequently, the boundary layer is expanded.

2.3.3 Impression of the Thermophoresis and Brownian Diffusion

Figs. 2.4$\,(a)$ − 2.4$\,(d)$ illustrate the significance of the thermo-migration N_t and Brownian diffusion N_b parameters on the thermal and mass transports. Due to the interaction of nanoparticles, molecules undergoes haphazard motion. This is mainly due to the impact of Brownian diffusion, which enhances the speed and momentum of particles and hence elevates the kinetic energy of the system. This abrupt rise in kinetic energy originates more irrational collisions of particles with an increment in temperature field $\theta(\eta)$ as illustrated in Figs. 2.4$\,(b)$; whereas, the concentration of particles $\phi(\eta)$ dwindles as seen in Fig. 2.4$\,(d)$. The mass transfer rate is intensified momentarily, and forcing the particles to relocate into a low concentrated zone by causing the system to endure the thermo-migration/thermophoresis. Here the more massive molecules experience the positive thermo-diffusion, *i.e.*, they move from a warmer to a colder zone. Hence, raising the thermal energy and concentration distribution as shown in Figs. 2.4$\,(a)$ and 2.4$\,(c)$.

2.3.4 Impression of the Prandtl and Schmidt Number

The impression of the Prandtl number Pr on the thermal distribution and Schmidt number Sc on the concentration field is highlighted in Figs. 2.5 (a) and 2.5 (b). The decline in the energy is owing to an endorsement in the Pr, which is the momentum diffusivity ν and thermal diffusivity α_{nf} ratio. Since for $1 < \mathrm{Pr} = 0.71, 6.13, 10.0, 20.0$, convection (momentum diffusivity ν) rules over conduction (thermal diffusivity α_{nf}) the thermal transportation is mainly due to convection, which causes decay in heat transfer rate. Moreover, by increasing the mass-momentum diffusion ratio, the mass diffusivity takes over the momentum diffusion, and the concentration distribution $\phi(\eta)$ is lessened, *i.e.*, it has an inverse relation with the concentration field as shown in Fig. 2.5 (b).

2.3.5 Impression of the Non-linear Thermal Radiation and Temperature Ratio

Figs. 2.6 (a) and 2.6 (b) presentes the impression of Rosseland's radiation parameter R_d and the wall-to-free stream temperature θ_w ratio. It is observed that with an increment in radiation coefficient R_d and temperature-ratio θ_w, the thermal transport rate and boundary layer rise. This is because the radiation generates more heat which raises the energy of the system and hence temperature correspondingly.

2.3.6 Impression of the Shear Stress

The zeros in shear-stress can be calculated at $\gamma = \pm 2.505, \pm 2.5182, \pm 2.5994$ for $M = 0.0$ and $k = 0.0, 0.01, 0.07$, respectively. Furthermore, for $k = 0.0, 0.01, 0.07$, $\gamma = 0$ and $M = 0.04$, the values in the graphs are noted to be 1.385469, 1.399778, and 1.485883. Fig. 2.7 verifies that when the ratio between shear rate b to strain rate a is negative, *i.e.*, $\gamma < 0$, for before-mentioned values of k there is no change in the coefficient of skin friction along the x-direction $\breve{f}''(0)$. But for $\gamma > 0$, when k increases $\breve{f}''(0)$ is also increased. It is also observed that when $\gamma < 0$, the coefficient of skin friction along the y-direction $\breve{g}''(0)$ enhances as k increases; whereas, for non-negative γ no apparent variation is noted. Note that the dotted lines in Fig. 2.7 represent their asymptotic behavior. It is evident from Fig. 2.7 that $\breve{f}''(0)$ reaches its asymptotic conduct; however, $\breve{g}''(0)$ does not.

2.3.7 Impression of the Displacement Thicknesses

The impressions of two-dimensional displacement thicknesses α and β are illustrated in Fig. 2.8(a). Both $\sqrt{\frac{a}{\nu}}\delta_x \equiv \alpha$ and $\sqrt{\frac{a}{\nu}}\delta_y \equiv \beta$ have identical values at $\gamma = 0$, $M = 0.2$, and $k = 0.0, 0.04, 0.07$ noted as, $0.5041, 0.4524$ and 0.4211, respectively. Moreover, by increasing the viscoelasticity k, α and β decreased for specific values of ratio between shear rate b to strain rate a. In Fig. 2.8(b), the consequences of 3D displacement thickness parameter δ_1 with γ are determined. It is discovered that for $\gamma = 0$ and $k = 0.0, 0.04, 0.07$, δ_1 attains maximum values, *i.e.*, 0.5432, 0.5077, and 0.4818, respectively. Additionally, we can perceive the behavior of these parameters for negative and non-negative values of γ.Fig. 2.8 (a) highlights that β started to increase when $-4 \leq \gamma \leq 6$; however, $\gamma > \pm 2.0$ we observed that with an increment in k, δ_1 decreased correspondingly as seen in Fig. 8(b). Besides, the dotted lines in Figs. 2.8(a) and 2.8(b) represent their asymptotic conduct. It is comprehended that the asymptotic value (dotted lines) of α is quite closer to its numerical value; whereas, β and δ_1 manifested contrary behavior.

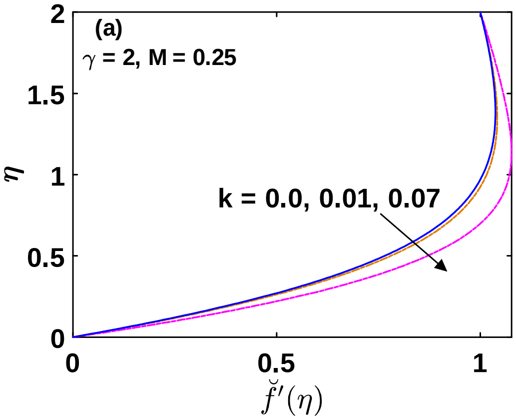

Fig. 2.2 (**a**) : Impression of k on $\breve{f}'(\eta)$.

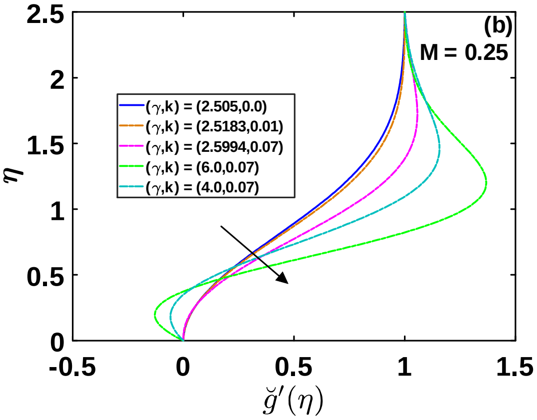

Fig. 2.2 (**b**) : Impression of k and γ on $\breve{g}'(\eta)$.

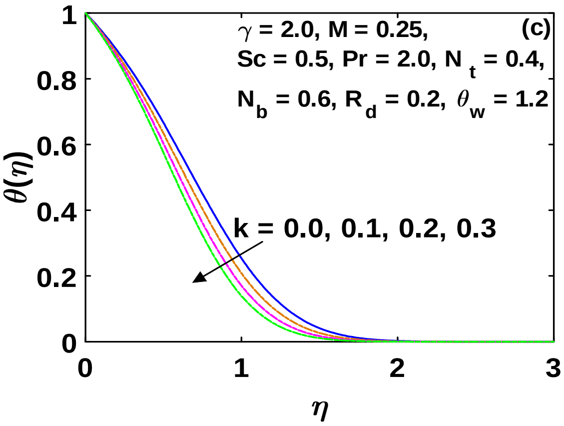

Fig. 2.2 (c) : Impression of k on $\theta(\eta)$.

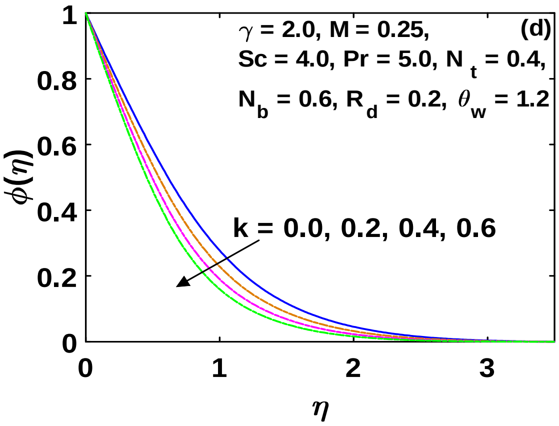

Fig. 2.2 (d) : Impression of k on $\phi(\eta)$.

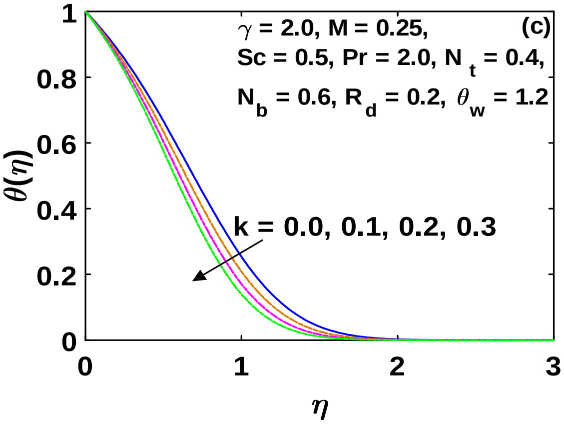

Fig. 2.2 (c) : Impression of k on $\theta(\eta)$.

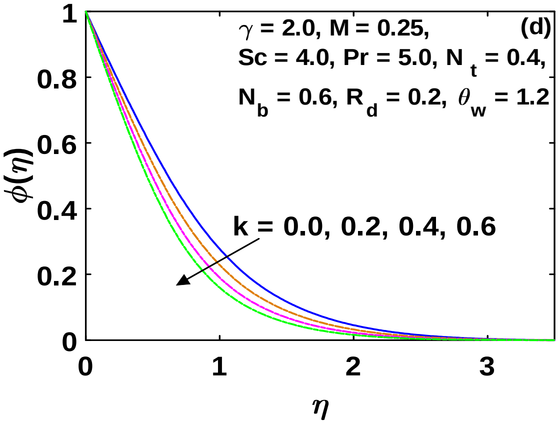

Fig. 2.2 (d) : Impression of k on $\phi(\eta)$.

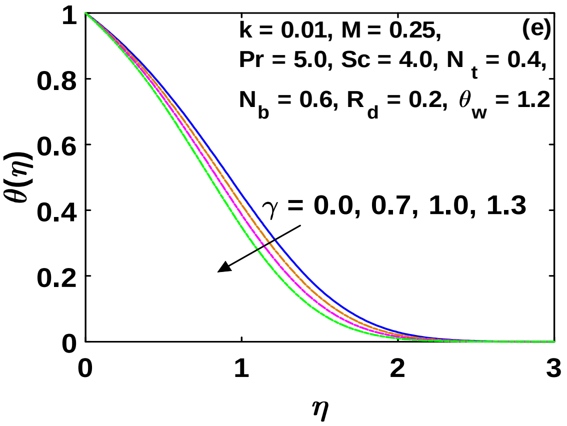

Fig. 2.2 (**e**) : Impression of γ on $\theta(\eta)$.

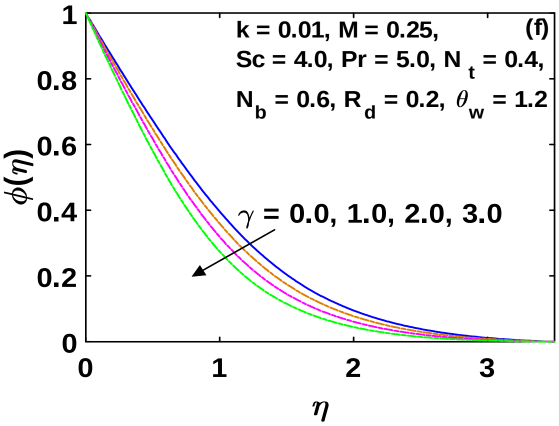

Fig. 2.2 (**f**) : Impression of γ on $\phi(\eta)$.

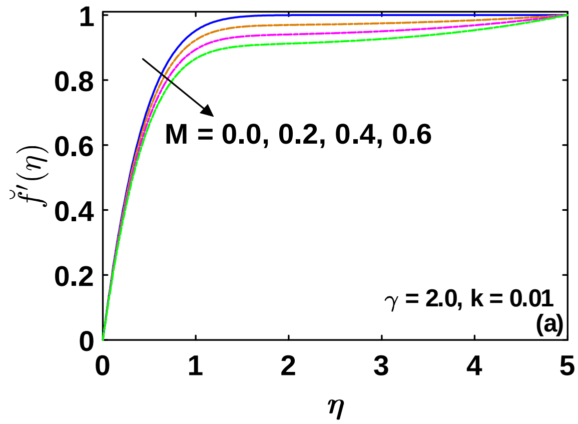

Fig. 2.3 (a) : Impression of M on $\breve{f}'(\eta)$.

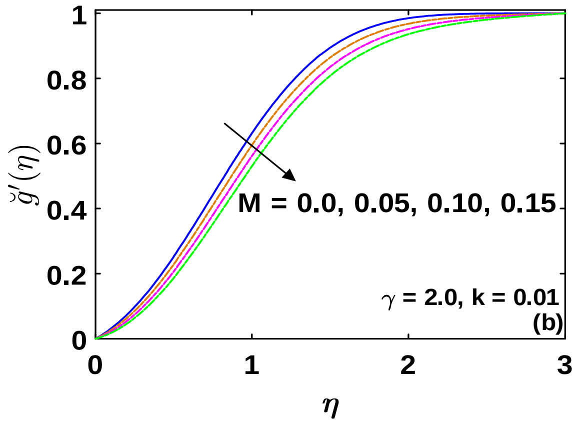

Fig. 2.3 (b) : Impression of M on $\breve{g}'(\eta)$.

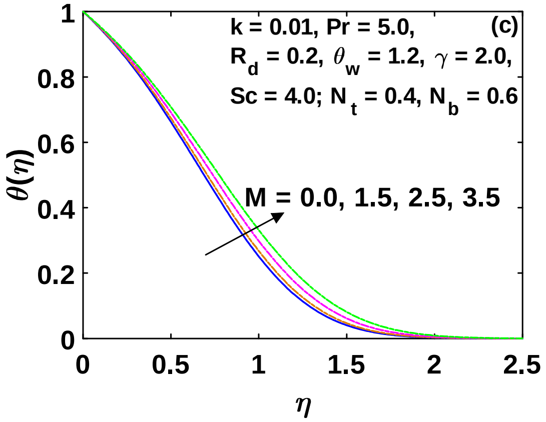

Fig. 2.3 (c) : Impression of M on $\theta(\eta)$.

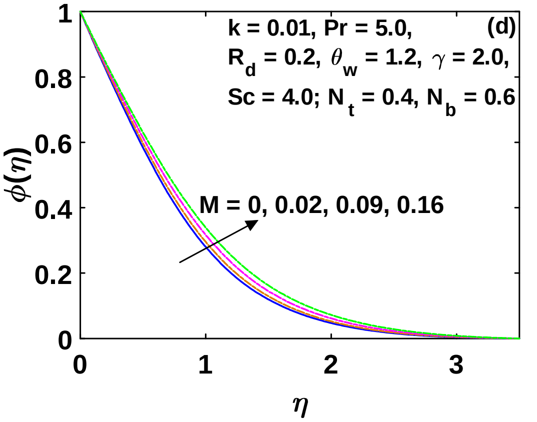

Fig. 2.3 (d) : Impression of M on $\phi(\eta)$.

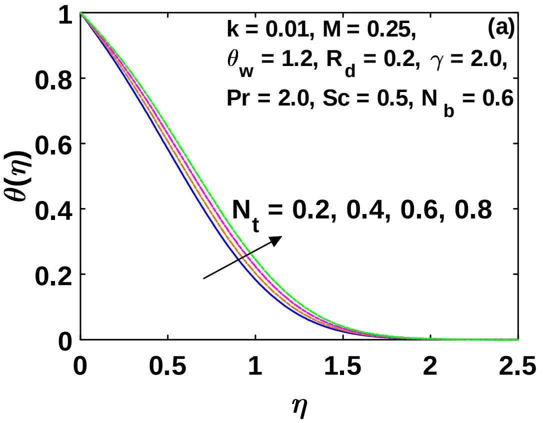

Fig. 2.4 (a) : Impression of N_t on $\theta(\eta)$.

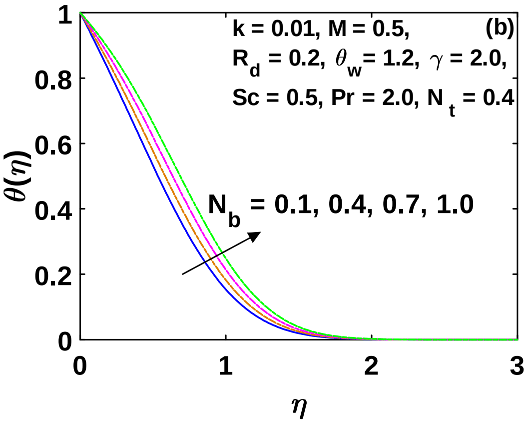

Fig. 2.4 (b) : Impression of N_b on $\theta(\eta)$.

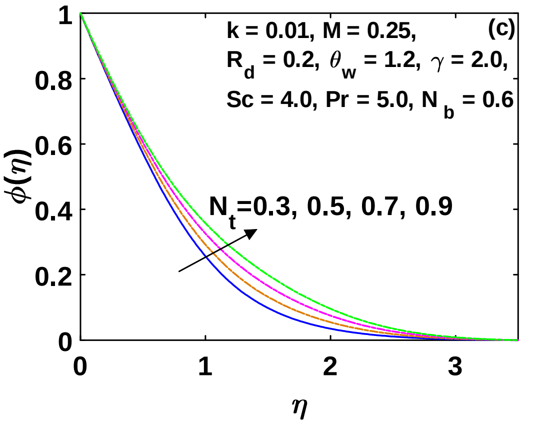

Fig. 2.4 (c) : Impression of N_t on $\phi(\eta)$.

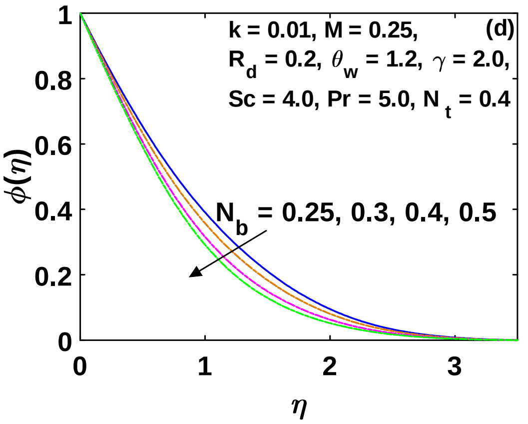

Fig. 2.4 (d) : Impression of N_b on $\phi(\eta)$.

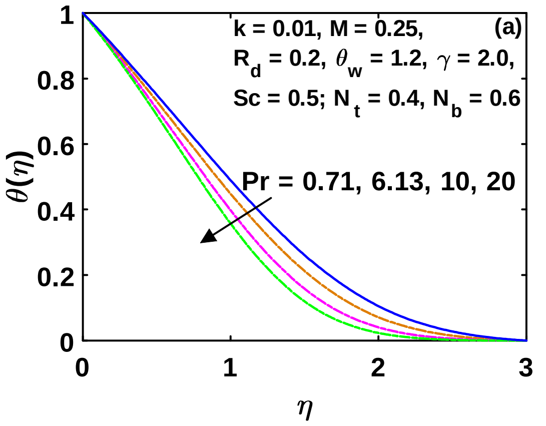

Fig. 2.5 (a) : Impression of Pr on $\theta(\eta)$.

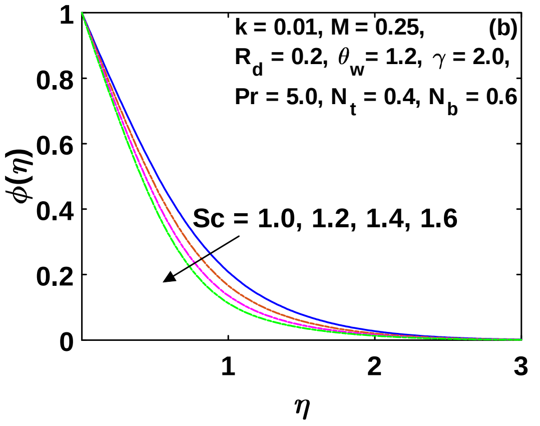

Fig. 2.5 (b) : Impression of Sc on $\phi(\eta)$.

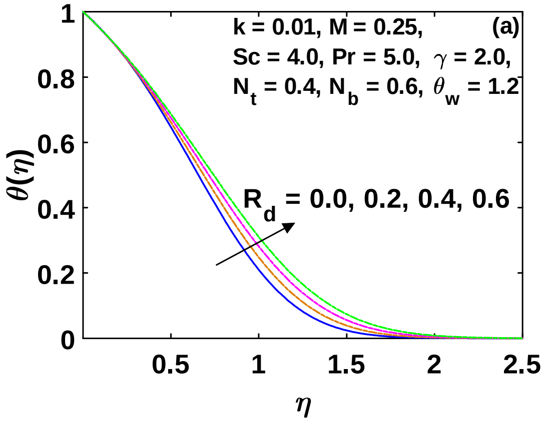

Fig. 2.6 (a) : Impression of R_d on $\theta(\eta)$.

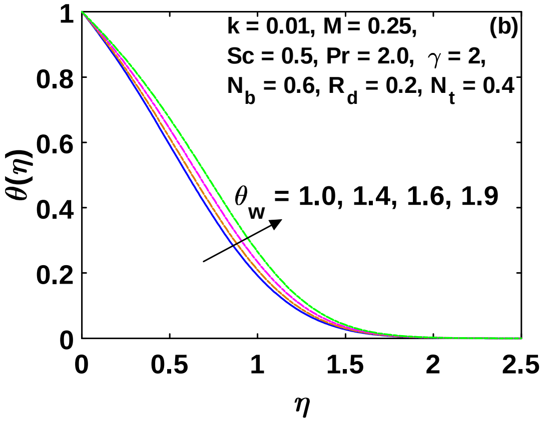

Fig. 2.6 (b) : Impression of θ_w on $\theta(\eta)$.

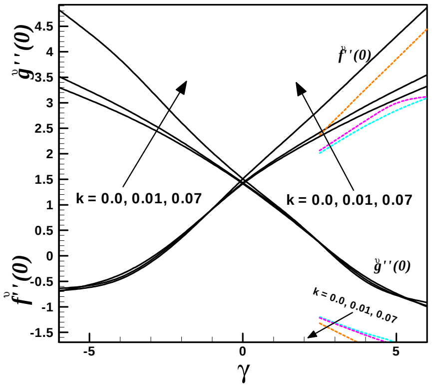

Fig. 2.7 : Impression of $\breve{f}''(0)$ and $\breve{g}''(0)$.

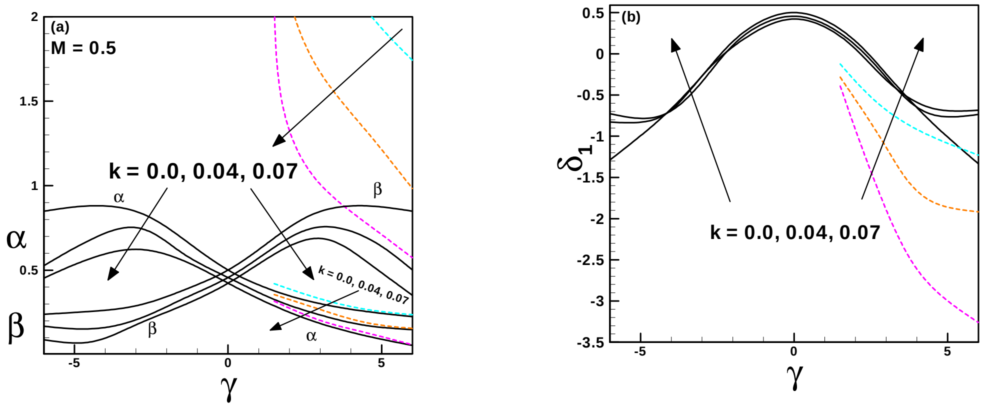

Fig. 2.8 (a) : Impression of α and β.

Fig. 2.8 (b) : Impression of δ_1.

2.4 Concluding Remarks

This article emphasized on the numerical and large-γ asymptotic solutions of non-axisymmetric Walter's B nanofluid flow near-stagnation zone. Contributions of the Rosseland non-linear radiation and MHD were scrutinized as well. Impression of the parameters involved were investigated for the flow, energy and concentration distribution. The numerical results and their asymptotic solutions were determined by practicing a built-in technique in Matlab® namely, bvp4c. Moreover, our acquired outcomes were consistent with the ones in literature. The observations made are summarized below.

- The viscoelasticity increased the flow along $\breve{f}'(\eta)$; however, reverse flow was observed for variation of γ and k with η in $\breve{g}'(\eta)$.
- The significance of viscoelasticity and magnetic field on skin-friction was inspected and it is revealed that for $\gamma \to \infty$, $\breve{f}''(0)$ reached its asymptotic behavior easily. However, $\breve{g}''(0)$ exhibited the contrary trend.
- The displacement thicknesses decreased with the increment of k for a specific value of the ratio of shear-to-strain rate. Graphs highlighted that as $\gamma \to \infty$, α reached its asymptotic value; whereas, same behavior was not depicted by β and δ_1.
- Temperature was boosted up for both the Soret impact and Brownian diffusion. However, fluid concentration was increased for the former and reduced for the latter.
- The role of non-linear thermal radiation on the temperature field was perceived to be increasing, which happens to thicken the BL.

Chapter 3

Jeffrey Nanofluid for Homann Stagnation-region with Solar Radiation Aspects

In this chapter, the Jeffrey's nanofluid flow for Homann's stagnation-point flow is modeled here, with time-independent free stream over an electrically conducting flow on a cylindrical disk. By deploying Buongiorno's model, the outcomes of the thermophoresis, Brownian diffusion, and solar radiation on the concentration and thermal boundary layer are also scrutinized. By similar transformation, the conservation equations are remodeled into non-linear ordinary differential equations. Furthermore, a comparison is made between the numerical and asymptotic solutions with large values of stress-to-strain-rate ratio, *i.e*, $\gamma = \left(\frac{b}{a}\right)$ for the parameters of displacement thicknesses and wall-shear stress. A finite-difference technique is utilized to numerically evaluate the calculations for the flow, energy, displacement thickness, skin drag, and concentration profiles. Also, the impact of Jeffrey's material parameters and magnetic field on displacement thickness is analyzed. It is discovered that when the shear-to-strain-rate ratio approaches infinity, the coefficient of skin friction along the x-axis attains its asymptotic behavior; whereas, along y-axis, it does not. Moreover, the two-dimensional displacement thickness along the x-axis is closer to get its asymptotic value when the γ approaches infinity, contrarily, for y-axis and the three-dimensional displacement thickness opposite trend is observed.

3.1 Mathematical Modeling

We considered the three-dimensional MHD Jeffrey's nanofluid stagnation-point flow for a cylindrical disk, along with the non-linear radiation. For heat transfer analysis of nanofluid we considered Buongiorno's model. At the wall of cylinder, fluid temperature with concentration is constant, *i.e.*, $\breve{T}(x,y,z) = \breve{T}_w$ and $\breve{C}(x,y,z) = \breve{C}_w$, respectively. By superposing $r\sin 2\vartheta$ and $r\cos 2\vartheta$ onto Homann's external potential flow, we stated the potential flow field in cylindrical coordinates system (r,ϑ,z) and transformed it into Cartesian coordinates (x,y,z). The potential field flow as obtained in § 2.1.1 of Chapter 2 is given as:

$$\mathbf{V} = [\breve{u},\breve{v},\breve{w}] = [x(a+b), y(a-b), -2az]. \tag{3.1}$$

The flow mechanism is given in Fig. 2.1. The conservation laws for steady incompressible flow are given in § 1.6 of Chapter 1. The Cauchy stress tensor $\boldsymbol{\tau}$ with true or extra stress tensor $\mathbf{S}$ is given in § 1.7.2. After determining the components of stress tensors from § 1.7.2 and employing the BL theory discussed in § 1.5 of Chapter 1 become:

$$\frac{\partial \breve{u}}{\partial x} + \frac{\partial \breve{v}}{\partial y} + \frac{\partial \breve{w}}{\partial z} = 0, \tag{3.2}$$

$$\begin{aligned}\breve{u}\frac{\partial \breve{u}}{\partial x} + \breve{v}\frac{\partial \breve{u}}{\partial y} + \breve{w}\frac{\partial \breve{u}}{\partial z} &= -\frac{1}{\rho}\frac{\partial p}{\partial x} - \frac{\sigma B_0^2 \breve{u}}{\rho} + \frac{\nu}{1+\lambda_1}\left[\frac{\partial^2 \breve{u}}{\partial z^2}\right.\\ \left.+\lambda_2\left(\breve{u}\frac{\partial^3 \breve{u}}{\partial x \partial z^2} + \frac{\partial \breve{u}}{\partial z}\frac{\partial^2 \breve{u}}{\partial x \partial z} + \breve{v}\frac{\partial^3 \breve{u}}{\partial y \partial z^2} + \frac{\partial \breve{v}}{\partial z}\frac{\partial^2 \breve{u}}{\partial y \partial z} + \breve{w}\frac{\partial^3 \breve{u}}{\partial z^3} + \frac{\partial \breve{w}}{\partial z}\frac{\partial^2 \breve{u}}{\partial z^2}\right)\right]&,\end{aligned} \tag{3.3}$$

$$\begin{aligned}\breve{u}\frac{\partial \breve{v}}{\partial x} + \tilde{v}\frac{\partial \breve{v}}{\partial y} + \tilde{w}\frac{\partial \breve{v}}{\partial z} &= -\frac{1}{\rho}\frac{\partial p}{\partial y} - \frac{\sigma B_0^2 \breve{v}}{\rho} + \frac{\nu}{1+\lambda_1}\left[\frac{\partial^2 \breve{v}}{\partial z^2}\right.\\ \left.+\lambda_2\left(\breve{u}\frac{\partial^3 \breve{v}}{\partial x \partial z^2} + \frac{\partial \breve{u}}{\partial z}\frac{\partial^2 \breve{v}}{\partial x \partial z} + \breve{v}\frac{\partial^3 \breve{v}}{\partial y \partial z^2} + \frac{\partial \breve{v}}{\partial z}\frac{\partial^2 \breve{w}}{\partial y \partial z} + \breve{w}\frac{\partial^3 \breve{v}}{\partial z^3} + \frac{\partial \breve{w}}{\partial z}\frac{\partial^2 \breve{v}}{\partial z^2}\right)\right]&,\end{aligned} \tag{3.4}$$

$$\breve{u}\frac{\partial \breve{T}}{\partial x} + \breve{v}\frac{\partial \breve{T}}{\partial y} + \breve{w}\frac{\partial \breve{T}}{\partial z} = \alpha_{nf}\frac{\partial^2 \breve{T}}{\partial z^2} - \frac{1}{(\rho c)_p}\frac{\partial q_T}{\partial z} + \frac{(\rho c)_{nf}}{(\rho c)_p}\left[D_B\frac{\partial \breve{T}}{\partial z}\frac{\partial \breve{C}}{\partial z} + \frac{D_T}{\breve{T}_\infty}\left(\frac{\partial \breve{T}}{\partial z}\right)^2\right], \tag{3.5}$$

$$\breve{u}\frac{\partial \breve{C}}{\partial x} + \breve{v}\frac{\partial \breve{C}}{\partial y} + \breve{w}\frac{\partial \breve{C}}{\partial z} = D_B\frac{\partial^2 \breve{C}}{\partial z^2} + \frac{D_T}{\breve{T}_\infty}\left(\frac{\partial^2 \breve{T}}{\partial z^2}\right). \tag{3.6}$$

The radiative thermal flux q_T [38] is evaluated by the diffusion approximation, interpreted as:

$$q_T = -\frac{4\sigma^*}{3k^*}\frac{\partial \breve{T}^4}{\partial z} = -\frac{16\sigma^* \breve{T}^3}{3k^*}\frac{\partial \breve{T}}{\partial z}. \tag{3.7}$$

Putting Eq. (3.7) in Eq. (3.5), we have

$$\breve{u}\frac{\partial \breve{T}}{\partial x} + \breve{v}\frac{\partial \breve{T}}{\partial y} + \breve{w}\frac{\partial \breve{T}}{\partial z} = \alpha_{nf}\frac{\partial^2 \breve{T}}{\partial z^2} + \frac{\partial}{\partial z}\left(\frac{16\sigma^* \breve{T}^3}{3k^*\left(\rho c\right)_p}\frac{\partial \breve{T}}{\partial z}\right) + \frac{(\rho c)_{nf}}{\left(\rho c\right)_p}\left[D_B\frac{\partial \breve{T}}{\partial z}\frac{\partial \breve{C}}{\partial z} + \frac{D_T}{\breve{T}_\infty}\left(\frac{\partial \breve{T}}{\partial z}\right)^2\right], \tag{3.8}$$

where B_0, σ, k^*, $\nu = \frac{\mu}{\rho}$, and σ^*denote the intensity of magnetic field, the electrical conductivity, the Stefan's constant, the kinematic viscosity, and the mean absorption coefficient, respectively.

The expressions of pressure gradient with velocity at free stream$\left(\breve{U}_\infty, \breve{V}_\infty\right)$ in Eqs. (3.3) and (3.4) are calculated by

$$\left.\begin{aligned} \breve{U}_\infty \tfrac{\sigma B_0^2}{\rho} + \breve{U}_\infty \tfrac{\partial \breve{U}_\infty}{\partial x} &= -\tfrac{1}{\rho}\tfrac{\partial p}{\partial x}, \\ \breve{V}_\infty \tfrac{\sigma B_0^2}{\rho} + \breve{V}_\infty \tfrac{\partial \breve{V}_\infty}{\partial y} &= -\tfrac{1}{\rho}\tfrac{\partial p}{\partial y}. \end{aligned}\right\} \tag{3.9}$$

3.1.1 Boundary Conditions

The problem is modeled with the free stream and no-slip condition, as:

$$\breve{u} = 0,\ \breve{v} = 0,\ \breve{w} = 0,\ \breve{T} = \breve{T}_w,\ \breve{C} = \breve{C}_w \quad \text{at } z = 0, \tag{3.10}$$

$$\breve{u} \to x\left(a + b\right),\ \breve{v} \to y\left(a - b\right),\ \breve{w} \to -2az,\ \breve{T} \to \breve{T}_\infty,\ \breve{C} \to \breve{C}_\infty \text{ as } z \to \infty. \tag{3.11}$$

3.1.2 Similarity Transformations

Employing the similarity transformation, used in § 2.1.4 which satisfies Eq. (3.2) . Substituting these equations we transformed Eqs. (3.4) – (3.6) into:

$$\begin{aligned} &\breve{f}''' + (1+\gamma)\left[(1+\lambda_1)\left(\breve{f}\breve{f}'' - \left(\breve{f}'\right)^2 + 1\right) + \beta_1\left(\breve{f}''^2 - \breve{f}\breve{f}^{iv}\right)\right] \\ &+ (1-\gamma)\left[(1+\lambda_1)\,\breve{g}\breve{f}'' - \beta_1\left(\breve{g}'\breve{f}''' + \breve{g}\breve{f}^{iv}\right)\right] - M^2\left(\breve{f}' - 1\right)(1+\lambda_1) = 0, \end{aligned} \tag{3.12}$$

$$\breve{g}''' + (1-\gamma)\left[(1+\lambda_1)\left(\breve{g}\breve{g}'' - (\breve{g}')^2 + 1\right) + \beta_1\left(\breve{g}''^2 - \breve{g}\breve{g}^{iv}\right)\right]$$
$$+ (1+\gamma)\left[(1+\lambda_1)\breve{f}\breve{g}'' - \beta_1\left(\breve{f}'\breve{g}''' + \breve{f}\breve{g}^{iv}\right)\right] - M^2(\breve{g}'-1)(1+\lambda_1) = 0, \tag{3.13}$$

$$\theta'' + \Pr\left[\breve{f}(1+\gamma)\theta' + \breve{g}(1-\gamma)\theta' + N_t(\theta')^2 + N_b(\theta'\phi')\right] +$$
$$R_d\left[3(1+\theta(\theta_w-1))^2(\theta_w-1)(\theta')^2 + (1+\theta(\theta_w-1))^3\theta''\right] = 0, \tag{3.14}$$

$$\phi'' + Sc\left[\breve{f}(1+\gamma) + \breve{g}(1-\gamma)\right]\phi' + \frac{N_t}{N_b}\theta'' = 0, \tag{3.15}$$

where a prime represents differentiation w.r.t η. The dimensionless parameters M, β_1, Pr, R_d, θ_w, N_t, Sc, and N_b are the magnetic parameter, the Deborah number, the Prandtl number, the non-linnear radiation parameter, the wall-to-ambient temperature-ratio, the thermodiffusion, the Schmidt number, and the Brownian motion coefficient, respectively.

$$\begin{aligned} M &= \sqrt{\frac{\sigma B_0^2}{a\rho}},\ \beta_1 = \lambda_2 a,\ \Pr = \frac{\nu}{\alpha_{nf}},\ R_d = \frac{16\sigma^*\breve{T}_\infty^3}{3k^*k_{nf}}, \\ \theta_w &= \frac{\breve{T}_w}{\breve{T}_\infty},\ N_t = \frac{(\rho c)_{nf}}{(\rho c)_p}\frac{D_T\left(\breve{T}_w - \breve{T}_\infty\right)}{\nu\breve{T}_\infty},\ Sc = \frac{\nu}{D_B}, \\ N_b &= \frac{(\rho c)_{nf}}{(\rho c)_p}\frac{D_B\left(\breve{C}_w - \breve{C}_\infty\right)}{\nu}. \end{aligned} \tag{3.16}$$

Using Eqs. (3.10) and (3.11), we obtain

$$\breve{f}(0) = 0,\ \breve{f}'(0) = 0,\ \breve{g}(0) = 0,\ \breve{g}'(0) = 0,\ \theta(0) = 1,\ \phi(0) = 1, \tag{3.17}$$
$$\breve{f}'(\infty) = 1,\ \breve{g}'(\infty) = 1,\ \phi(\infty) = 0,\ \theta(\infty) = 0. \tag{3.18}$$

3.1.3 Shear Stress

Wall-shear stress can be computed

$$\boldsymbol{\tau} = \left[(\tau_{xz})\,\mathbf{i} + (\tau_{yz})\,\mathbf{j}\right|_{z=0}, \tag{3.19}$$

where

$$
\begin{aligned}
\left[\tau_{xz}\right|_{z=0} &= \frac{\mu a^{\frac{3}{2}}\nu^{-\frac{1}{2}}\left(1+\gamma\right)x}{\left(1+\lambda_1\right)}\left[\breve{f}''\left(0\right)+\beta\left\{\left(1+\gamma\right)\left(\breve{f}'\left(0\right)\breve{f}''\left(0\right)-\breve{f}\left(0\right)\breve{f}'''\left(0\right)\right)\right.\right. \\
&\quad \left.\left.-\left(1-\gamma\right)\breve{g}\left(0\right)\breve{f}'''\left(0\right)\right\}\right], \qquad (3.20) \\
\left[\tau_{yz}\right|_{z=0} &= \frac{\mu a^{\frac{3}{2}}\nu^{-\frac{1}{2}}\left(1-\gamma\right)y}{\left(1+\lambda_1\right)}\left[\breve{g}''\left(0\right)+\beta\left\{\left(1-\gamma\right)\left(\breve{g}'\left(0\right)\breve{g}''\left(0\right)-\breve{g}\left(0\right)\breve{g}'''\left(0\right)\right)\right.\right. \\
&\quad \left.\left.-\left(1+\gamma\right)\breve{f}\left(0\right)\breve{g}'''\left(0\right)\right\}\right]. \qquad (3.21)
\end{aligned}
$$

3.1.4 Displacement Thicknesses

The 2D and 3D displacement thicknesses δ_x, δ_y and δ_1, respectively, are calculated (see Davey [13] and Lighthill [40])

$$\sqrt{\frac{a}{\nu}}\delta_x = \int_0^\infty \left[1-\frac{\breve{u}}{\breve{U}_\infty}\right]d\eta = \int_0^\infty \left[1-\breve{f}'\left(\eta\right)\right]d\eta, \qquad (3.22)$$

$$\sqrt{\frac{a}{\nu}}\delta_y = \int_0^\infty \left[1-\frac{\breve{v}}{\breve{V}_\infty}\right]d\eta = \int_0^\infty \left[1-\breve{g}'\left(\eta\right)\right]d\eta, \qquad (3.23)$$

and

$$\delta_1 = \frac{\left(1+\gamma\right)\alpha+\left(1-\gamma\right)\beta}{2}. \qquad (3.24)$$

It is perceived that, δ_x and δ_y tend to zero as γ proceed towards infinity; however, δ_1 goes to $-\infty$ for the same range of γ. These results can be seen in Figs. $3.9\left(a\right)$ and $3.9\left(b\right)$.

3.2 Numerical Solutions

The numerical outcomes for the equations obtained are computed by a finite-difference based technique-bvp4c in Matlab®. The high-ordered equations are turned into first-order ODEs by introducing a set of variables including corresponding boundary conditions, values for the constants involved, and an initial guess as discussed in § 1.9 of Chapter 1.

3.2.1 Regular Perturbation Expansion

To determine the solution of the problem, perturbation expansion is adopted. The target of this section is to calculate the numerical results for the flow. Since Eqs. (3.12) and (3.13) are the fourth-order differential equations and boundary conditions are not adequate to compute the solution; therefore, we adopt the approach used by Beard [39] . To obtain the approximate solution, we take the Deborah number very small, i.e., $\beta_1 \ll 1$.

$$\breve{f}\left(\eta\right) = \breve{f}_0\left(\eta\right) + \beta_1 \breve{f}_1\left(\eta\right) + \beta_1^2 \breve{f}_2\left(\eta\right) + \cdots , \tag{3.25}$$

$$\breve{g}\left(\eta\right) = \breve{g}_0\left(\eta\right) + \beta_1 \breve{g}_1\left(\eta\right) + \beta_1^2 \breve{g}_2\left(\eta\right) + \cdots . \tag{3.26}$$

Putting Eqs. (3.25) and (3.26) in Eqs. (3.12) and (3.13), β_1^0 and β_1 coefficients are:

$$\breve{f}_0''' + \left(1+\lambda_1\right)\left[\left(1+\gamma\right)\left(\breve{f}_0\breve{f}_0'' - \left(\breve{f}_0'\right)^2 + 1\right) + \left(1-\gamma\right)\breve{g}_0\breve{f}_0'' - M^2\left(\breve{f}_0' - 1\right)\right] = 0, \tag{3.27}$$

$$\breve{g}_0''' + \left(1+\lambda_1\right)\left[\left(1-\gamma\right)\left(\breve{g}_0\breve{g}_0'' - \left(\breve{g}_0'\right)^2 + 1\right) + \left(1+\gamma\right)\breve{f}_0\breve{g}_0'' - M^2\left(\breve{g}_0' - 1\right)\right] = 0, \tag{3.28}$$

$$\begin{aligned} &\breve{f}_1''' + \left(1+\gamma\right)\left[\left(\breve{f}_0''\right)^2 - \breve{f}_0\breve{f}_0^{iv} + \left(1+\lambda_1\right)\left(\breve{f}_1\breve{f}_0'' + \breve{f}_0\breve{f}_1'' - 2\breve{f}_0'\breve{f}_1'\right)\right] \\ &+ \left(1-\gamma\right)\left[-\breve{g}_0'\breve{f}_0''' - \breve{g}_0\breve{f}_0^{iv} + \left(1+\lambda_1\right)\left(\breve{g}_0\breve{f}_1'' + \breve{g}_1\breve{f}_0''\right)\right] - M^2\left(1+\lambda_1\right)\breve{f}_1' = 0, \end{aligned} \tag{3.29}$$

$$\begin{aligned} &\breve{g}_1''' + \left(1-\gamma\right)\left[\left(\breve{g}_0''\right)^2 - \breve{g}_0\breve{g}_0^{iv} + \left(1+\lambda_1\right)\left(\breve{g}_1\breve{g}_0'' + \breve{g}_0\breve{g}_1'' - 2\breve{g}_0'\breve{g}_1'\right)\right] \\ &+ \left(1+\gamma\right)\left[-\breve{f}_0'\breve{g}_0''' - \breve{f}_0\breve{g}_0^{iv} + \left(1+\lambda_1\right)\left(\breve{f}_0\breve{g}_1'' + \breve{f}_1\breve{g}_0''\right)\right] - M^2\left(1+\lambda_1\right)\breve{g}_1' = 0. \end{aligned} \tag{3.30}$$

The boundary conditions for above equations are

$$\breve{f}_0\left(0\right) = 0,\ \breve{f}_0'\left(0\right) = 0,\ \breve{f}_0'\left(\infty\right) = 1,\ \breve{g}_0\left(0\right) = 0,\ \breve{g}_0'\left(0\right) = 0,\ \breve{g}_0'\left(\infty\right) = 1, \tag{3.31}$$

$$\breve{f}_1\left(0\right) = 0,\ \breve{f}_1'\left(0\right) = 0,\ \breve{f}_1'\left(\infty\right) = 0,\ \breve{g}_1\left(0\right) = 0,\ \breve{g}_1'\left(0\right) = 0,\ \breve{g}_1'\left(\infty\right) = 0. \tag{3.32}$$

Using Eqs. (3.25) and (3.26) in Eqs. (3.22) and (3.23), we get perturbed equations for 2D displacement thicknesses.

$$\sqrt{\frac{a}{\nu}}\delta_x = \int_0^\infty \left[1 - \breve{f}_0'(\eta) - \beta_1 \breve{f}_1'(\eta)\right] d\eta \equiv \alpha, \tag{3.33}$$

$$\sqrt{\frac{a}{\nu}}\delta_y = \int_0^\infty \left[1 - \breve{g}_0'(\eta) - \beta_1 \breve{g}_1'(\eta)\, d\eta\right] \equiv \beta. \tag{3.34}$$

Here α and β denote the 2D displacement thickness parameters.

3.2.2 Asymptotic for $\gamma \gg 1$

By changing variables, the asymptotic conduct of the solution is determined for large shear-to-strain-rate ratio as:

$$\breve{f}(\eta) = \epsilon \breve{F}(\zeta), \text{ and } \breve{g}(\eta) = \epsilon \breve{G}(\zeta), \tag{3.35}$$

with

$$\zeta = \eta\epsilon^{-1}, \ \beta_1 = \epsilon^3, \text{ and } \epsilon = \gamma^{-\frac{1}{2}} \ll 1. \tag{3.36}$$

From these transformed variables, Eqs. (3.12) and (3.13) become:

$$\begin{aligned} &\breve{F}''' + \left(\epsilon^2 + 1\right)\left[(1+\lambda_1)\left(\breve{F}\breve{F}'' - \breve{F}'^2 + 1\right) + \epsilon\left(\breve{F}''^2 - \breve{F}\breve{F}^{iv}\right)\right] \\ &+ \left(\epsilon^2 - 1\right)\left[(1+\lambda_1)\breve{G}\breve{F}'' - \epsilon\left(\breve{G}'\breve{F}''' + \breve{G}\breve{F}^{iv}\right)\right] - \epsilon^2 M^2 (1+\lambda_1)\left(\breve{F}' - 1\right) = 0, \end{aligned} \tag{3.37}$$

$$\begin{aligned} &\breve{G}''' + \left(\epsilon^2 - 1\right)\left[(1+\lambda_1)\left(\breve{G}\breve{G}'' - \breve{G}'^2 + 1\right) + \epsilon\left(\breve{G}''^2 - \breve{G}\breve{G}^{iv}\right)\right] \\ &+ \left(\epsilon^2 + 1\right)\left[(1+\lambda_1)\breve{F}\breve{G}'' - \epsilon\left(\breve{F}'\breve{G}''' + \breve{F}\breve{G}^{iv}\right)\right] - \epsilon^2 M^2 (1+\lambda_1)\left(\breve{G}' - 1\right) = 0, \end{aligned} \tag{3.38}$$

where a prime in Eqs. (3.37) and (3.38) denote differentiation w.r.t ζ. By using regular perturbation, we get

$$\breve{F}(\zeta) = \breve{F}_0(\zeta) + \epsilon \breve{F}_1(\zeta) + \epsilon^2 \breve{F}_2(\zeta) + \cdots, \tag{3.39}$$

$$\breve{G}(\zeta) = \breve{G}_0(\zeta) + \epsilon \breve{G}_1(\zeta) + \epsilon^2 \breve{G}_2(\zeta) + \cdots. \tag{3.40}$$

Using Eqs. (3.39) and (3.40) in Eqs. (3.37) and (3.38) , and equating ϵ^0 and ϵ^1

$$\breve{F}_0''' + (1+\lambda_1)\left[\left(\breve{F}_0 - \breve{G}_0\right)\breve{F}_0'' + 1 - \left(\breve{F}_0'\right)^2\right] = 0, \tag{3.41}$$

$$\breve{G}_0''' - (1+\lambda_1)\left[\left(\breve{G}_0 - \breve{F}_0\right)\breve{G}_0'' + 1 - \left(\breve{G}_0'\right)^2\right] = 0, \tag{3.42}$$

$$\begin{aligned} &\breve{F}_1''' + (1+\lambda_1)\Big[\breve{F}_0\breve{F}_1'' + \breve{F}_1\breve{F}_0'' - 2\breve{F}_0'\breve{F}_1' \\ &+ \left(\breve{F}_0''\right)^2 - \breve{F}_0\breve{F}_0^{iv} + \breve{G}_0\breve{F}_1'' - \breve{G}_1\breve{F}_0'' - \breve{G}_0'\breve{F}_0''' - \breve{G}_0\breve{F}_0^{iv}\Big] = 0, \end{aligned} \tag{3.43}$$

$$\begin{aligned} &\breve{G}_1''' - (1+\lambda_1)\Big[\breve{G}_0\breve{G}_1'' + \breve{G}_1\breve{G}_0'' - 2\breve{G}_0'\breve{G}_1' \\ &+ \left(\breve{G}_0''\right)^2 - \breve{G}_0\breve{G}_0^{iv} + \breve{F}_0\breve{G}_1'' + \breve{F}_1\breve{G}_0'' - \breve{F}_0'\breve{G}_0''' - \breve{F}_0\breve{G}_0^{iv}\Big] = 0, \end{aligned} \tag{3.44}$$

with respective boundary conditions

$$\begin{aligned} \breve{F}_0(0) &= 0,\ \breve{F}_0'(0) = 0,\ \breve{F}_0'(\infty) = 1,\ \breve{G}_0(0) = 0,\ \breve{G}_0'(0) = 0,\ \breve{G}_0'(\infty) = 1, \\ \breve{F}_1(0) &= 0,\ \breve{F}_1'(0) = 0,\ \breve{F}_1'(\infty) = 0,\ \breve{G}_1(0) = 0,\ \breve{G}_1'(0) = 0,\ \breve{G}_1'(\infty) = 0. \end{aligned} \tag{3.45}$$

Large-γ Shear Stress

Shear stress parameters for large-γ lower and first-order behaviors with the impression of magnetic field are determined by utilizing Eqs. (3.35) and (3.36), given as:

$$\breve{f}''(0) \sim \left[\breve{F}_0''(0) + \beta_1\gamma\breve{F}_1''(0)\right]\gamma^{\frac{1}{2}}, \tag{3.46}$$

$$\breve{g}''(0) \sim \left[\breve{G}_0''(0) + \beta_1\gamma\breve{G}_1''(0)\right]\gamma^{\frac{1}{2}}. \tag{3.47}$$

Large-γ Displacement Thicknesses

Let $\alpha = \epsilon\alpha^*$and $\beta = \epsilon\beta^*$ be the displacement thickness parameters, we get

$$\alpha^* = \int\limits_0^\infty \left[1 - \breve{F}_0'(\zeta)\right] d\zeta - \epsilon\int\limits_0^\infty \breve{F}_1'(\zeta)\, d\zeta = \alpha_0^* + \epsilon\alpha_1^*, \tag{3.48}$$

$$\beta^* = \int\limits_0^\infty \left[1 - \breve{G}_0'(\zeta)\right] d\zeta - \epsilon\int\limits_0^\infty \breve{G}_1'(\zeta)\, d\zeta = \beta_0^* + \epsilon\beta_1^*. \tag{3.49}$$

with

$$\alpha \sim \gamma^{-\frac{1}{2}}\alpha^* \text{ and } \beta \sim \gamma^{-\frac{1}{2}}\beta^*, \tag{3.50}$$

and

$$\delta^* \sim \frac{(1+\gamma)\,\alpha^* + (1-\gamma)\,\beta^*}{2\gamma^{\frac{1}{2}}}. \tag{3.51}$$

3.2.3 Results Authentication

From inspection of Eqs. (3.12) and (3.13) , it is noted that they are reflexive symmetries, *i.e.*,

$$\breve{f}(\eta, -\gamma) = \breve{g}(\eta, \gamma)\,, \text{ and } \breve{g}(\eta, -\gamma) = \breve{f}(\eta, \gamma)\,. \tag{3.52}$$

Moreover, by using $\beta_1 = k$ and $\lambda_1 = M = 0$ in Eqs. (3.12) and (3.13) , Walter's B fluid flow [6] is retrieved. We can also get values of 2D displacement thickness parameters α and β for zeroth order as $\alpha_0^* = 0.610$, $\beta_0^* = 3.4384$ and first order as $\alpha_1^* = -0.9984$, $\beta_1^* = -3.9349$. Putting $\gamma = 1$ and $\lambda_1 = \beta_1 = M = 0$ in Eqs. (3.12) and (3.13) , recovers the Hiemenz [10] equation. Also, when we substitute $\gamma = \lambda_1 = \beta_1 = M = 0$ in Eqs. (3.12) and (3.13) , we can get the axisymmetric Homann [11] flow equation, *i.e.*, $\breve{f}(\eta) = \breve{g}(\eta)$. When $\lambda_1 = \beta_1 = M = 0$ in Eqs. (3.12) and (3.13) , the Newtonian model given by Weidman [18] is obtained. The zero$^{\text{th}}$ ordered values of 2D displacement thicknesses are computed for a special case as $\alpha_0^* = 0.610$, $\beta_0^* = 3.4384$. The numerical outcomes for asymptotic values are compared with Refs. [6] and [18] in Table 1.

Table 3.1 : Asymptotic behavior of Shear Stress parameters.

	Ref. [6]	**Refs.** [18] and [13]	**Present**
	$M=\lambda_1=0,\ \beta_1=k,$	$M=\beta_1=\lambda_1=0$	$M=\lambda_1=0,\ \beta_1=k,$
$\breve{F}_0''(0)$	1.2729	1.2729	1.2729
$\breve{G}_0''(0)$	-0.8112	-0.8112	-0.8112
$\breve{F}_1''(0)$	1.2805		1.2805
$\breve{G}_1''(0)$	-0.4435		-0.4435

3.3 Graphical Discussion

The case of Jeffrey's nanofluid flow for non-axisymmetric Homann flow in the stagnation zone is studied in this article. To compute and plot the numerical solutions, we applied a finite difference based method, bvp4c in Matlab®, which utilizes the Lobatto formula as discussed in § 1.9. The numerical outcomes are calculated for the fluid velocity, displacement thickness, wall-shear stress, concentration, and temperature fields for the associated parameters, *i.e.,* the magnetic parameter M, the relaxation-to-retardation time ratio λ_1, the Prandtl number Pr, the Deborah number β_1, the Brownian motion parameter N_b, the Schmidt number Sc, the shear-to-strain rate ratio γ, the temperature-ratio θ_w, and the thermophoretic parameter N_t.

3.3.1 Impression of the Deborah Number

Figs. $3.1\,(a) - 3.1\,(d)$ illustrate the outcomes of the Deborah number β_1 on the fluid flow, temperature, and concentration field. The retardation-time λ_2 signifies the delay or obstruction in response to the stress, and often utilized in the creep test as shown in Fig. $3.1\,(a)$. In Fig. $3.1\,(b)$ the flow field along y-axis is inclined. It is noted that with an increment in the values of β_1 from 0.0 to $0.8, 1.6$ and 2.4, the thermal transport is lessened and the boundary layer is contracted as shown in Fig. $3.1\,(c)$. Furthermore, Fig. $3.1\,(d)$ presents the impact of β_1 on the mass tansport rate. It is preceived that $\phi\,(\eta)$ is declined by enhancing β_1 from 0.0 to 0.3.

3.3.2 Impression of the Magnetic Field

Figs. $3.2\,(a) - 3.2\,(d)$ give the contribution of magnetic field on the velocities $\breve{f}'(\eta)$, $\breve{g}'(\eta)$, fluid temperature $\theta(\eta)$, and concentration $\phi(\eta)$. It is discerned that by raising the magnetic field M, the concentration and temperature fields are elevated. However, owing to *Lorentz/electromagnetic force* created due to the magnetic field, the flow experienced a resisting force, and the velocity profile is lessened by enhancing the values of M. Additionally, the impression on the thermal and mass boundary layer is determined to be thickening.

3.3.3 Impression of the Shear-to-Strain-Rate Ratio

Figs. $3.3\,(a) - 3.3\,(d)$ visualize the impression of γ on the flow, energy and mass transportation. By enlarging γ, the shear rate b over rules the strain rate a; whereas decrement in γ raises the strain rate a. In Fig. $3.3\,(a)$ the flow along x-axis is enhanced; however along y-axis is declined significantly as shown in Fig. $3.3\,(b)$. It is perceived that the thermal and mass transport distribution decayed with an increment in γ.

3.3.4 Impression of the Relaxation-to-Retardation Time Ratio

In Figs. $3.4\,(a) - 3.4\,(d)$, variation of the ratio between relaxation to retardation time λ_1 with η is shown. Relaxation time reveals time to mitigate stress in polymers under constant strain. Velocities are enhanced by increasing λ_1 as seen in Figs. $3.4\,(a)$ and $3.4\,(b)$. However, temperature $\theta(\eta)$ is reduced significantly. The same behavior is noticed for the concentration profile, given in Figs. $3.4\,(c)$ and $3.4\,(d)$, repectively.

3.3.5 Impression of the Radiation and Temperature Ratio

In Figs. $3.5\,(a)$ and $3.5\,(b)$ it is shown that with an increment in R_d and θ_w, the temperature profile along with the boundary layer is elevated. Since because of the Rosseland approximation for radiation, more heat and energy is generated due to the greater conductivity of nanofluid, and it raises the fluid temperature/energy correspondingly as shown in Figs. $3.5\,(a)$ and $3.5\,(b)$.

3.3.6 Impression of Prandtl Number and Schmidt Number

Fig. 3.6 (a) presents the impact of Prandtl number, *i.e.,* the momentum-to-thermal diffusivity ratio on the temperature field. It is determined that the energy is reduced by enlarging Pr . Fig. 3.6 (b) shows the consequences of Schmidt number on the fluid concentration $\phi(\eta)$. It describes the mass-momentum transfer rate and has an inverse relation with the concentration profile.

3.3.7 Impression of the Thermophoresis and Brownian Diffusion

Figs. 3.7 (a) and 3.7 (b) determine the contribution of the thermophoresis and Brownian diffusion on the temperature. It is seen that fluid temperature rises for larger values of both N_b and N_t. The variations of N_b and N_t are presented for concentration field in Figs. 3.7 (c) and 3.7 (d) . For enhancing the value of N_b, the concentration field is depreciated; whereas, for N_t, fluid concentration enhances significantly. Since the interaction of nanoparticles causes random motion of the particles, which transpires heat conduction, the kinetic energy of the system is magnified, which significantly affects the Brownian motion. However, due to thermophoresis, those molecules which have higher kinetic energy motivates the particles to migrate towards the region of lower temperature. Therefore, the concentration boundary layer is thickened.

3.3.8 Impression of the Shear Stress

The zeros in shear stress can be determined at $\gamma = \pm 2.505, \pm 2.5182, \pm 2.5994$ for $\beta_1 = M = \lambda_1 = 0$. Additionally, for selected values of β_1 at $\gamma = 0$, $\lambda_1 = 0.2$, and $M = 0.04$, the values in the graphs are noted to be $1.385435, 1.495094$, and 1.591860. Fig. 3.8 verified that for different values of β_1, there is no apparent change seen in the coefficient of skin friction along the x-direction $\breve{f}''(0)$ when $\gamma < 0$ (negative). But for non-negative value of ratio between shear rate b to strain rate a, *i.e.*, $0 < \gamma \leq 5$ with an increment in β_1, $\breve{f}''(0)$ is also enhanced. It is also observed that when γ is negative, the coefficient of skin friction along the y-direction $\breve{g}''(0)$ inclined as values of β_1 increased; whereas for $0 < \gamma \leq 5$, no apparent change is noted. Moreover, the dotted lines in Fig. 3.8 represent their asymptotic behavior. It is apparent from Fig. 3.8 that $\breve{f}''(0)$ gains its asymptotic conduct; however, $\breve{g}''(0)$ does not.

3.3.9 Impression of the Displacement Thicknesses

The impressions of $\sqrt{\frac{a}{\nu}}\delta_x \equiv \alpha$ and $\sqrt{\frac{a}{\nu}}\delta_y \equiv \beta$ are illustrated in Fig. $3.9\,(a)$. Both α and β have similar values at $\gamma = 0$ and $\beta_1 = 0.0, 0.02, 0.2$ noted as, $0.5251, 0.5032$ and 0.4519, respectively. Furthermore, with an increment in the Deborah number β_1, these parameters (α and β) both are reduced for particular values of shear-to-strain rate ratio γ. In Fig. $3.9\,(b)$, the impacts of 3D displacement thickness parameter δ_1 with γ are determined. It is discovered that for $\gamma = 0$ and $\beta_1 = 0.0, 0.02, 0.2$, δ_1 attained maximum values, *i.e.*, 0.5251, 0.5032 and 0.4519, respectively. Furthermore, another way to read these graphs is to note the behavior of these parameters for negative and non-negative values of γ. For $\gamma > \pm 2.0$, we observed the value of δ_1 correspondingly declined by enhancing β_1 as shown in Fig. $3.9\,(b)$. However, α started to decline significantly from $-4 \leq \gamma \leq 6$ as displayed in Fig. $3.9\,(a)$. Moreover, α closer to its asymptotic value (dotted lines); whereas, β and δ_1 exhibited opposite behavior.

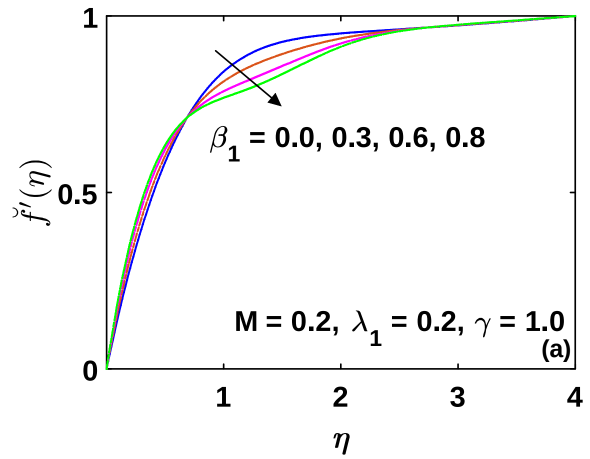

Fig. 3.1 (a) : Impression of β_1 on $\breve{f}'(\eta)$.

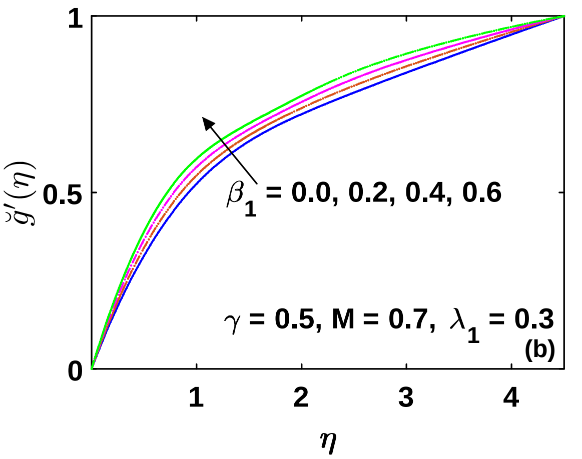

Fig. 3.1 (b) : Impression of β_1 on $\breve{g}'(\eta)$.

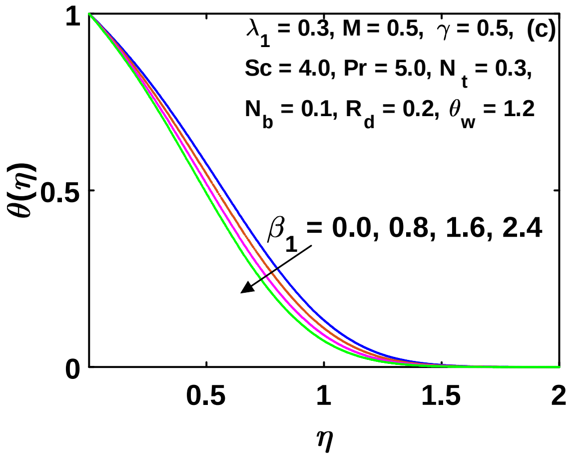

Fig. 3.1 (c) : Impression of β_1 on $\theta(\eta)$.

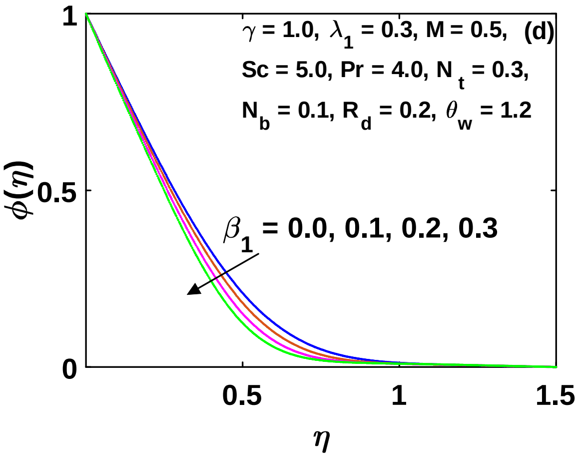

Fig. 3.1 (d) : Impression of β_1 on $\phi(\eta)$.

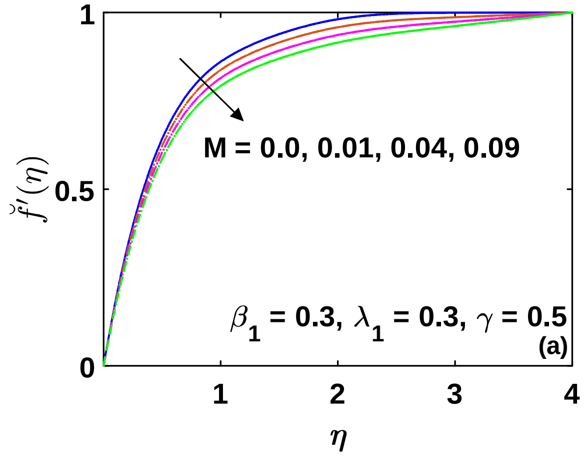

Fig. 3.2 (a) : Impression of M on $\breve{f}'(\eta)$.

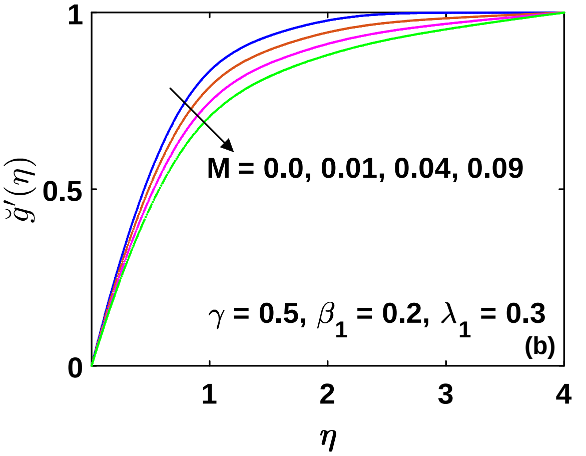

Fig. 3.2 (b) : Impression of M on $\breve{g}'(\eta)$.

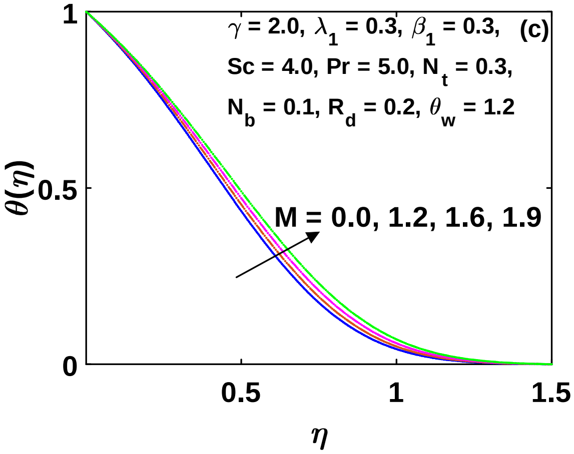

Fig. 3.2 (c) : Impression of M on $\theta(\eta)$.

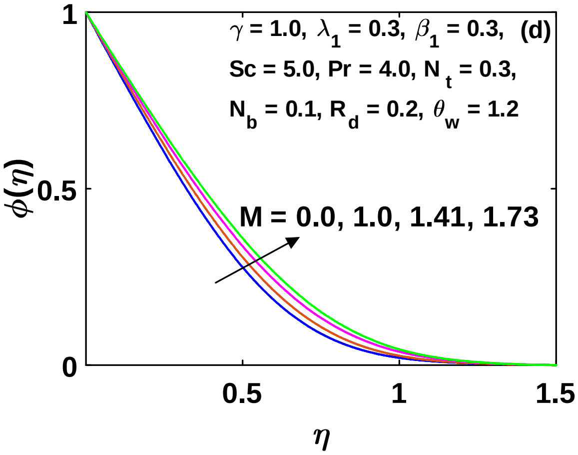

Fig. 3.2 (d) : Impression of M on $\phi(\eta)$.

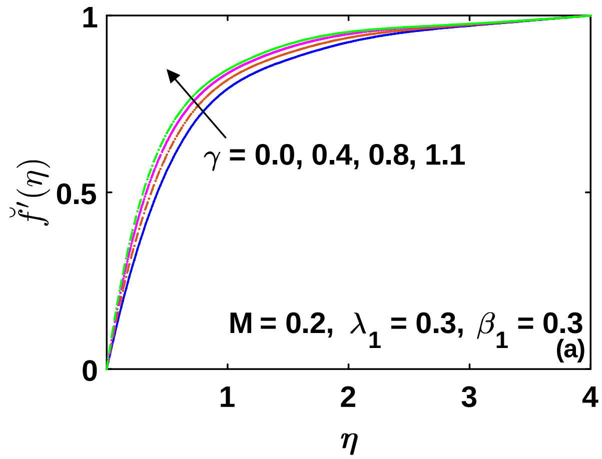

Fig. 3.3 (a) : Impression of γ on $\breve{f}'(\eta)$.

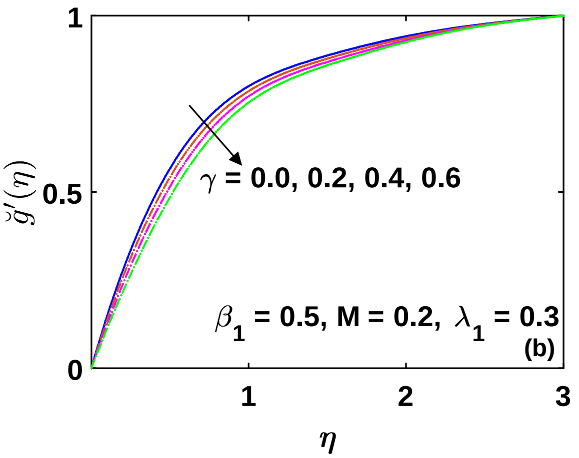

Fig. 3.3 (b) : Impression of γ on $\breve{g}'(\eta)$.

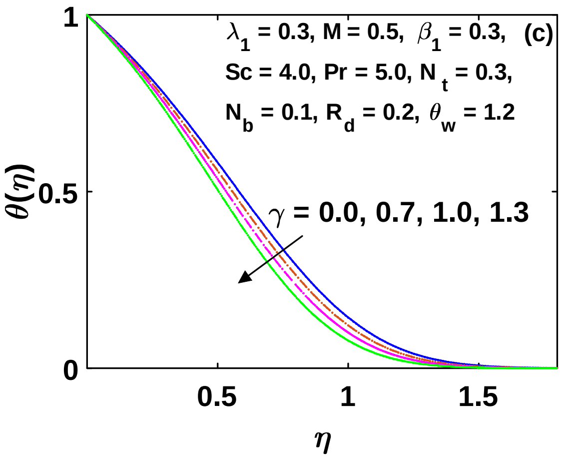

Fig. 3.3 (c) : Impression of γ on $\theta(\eta)$.

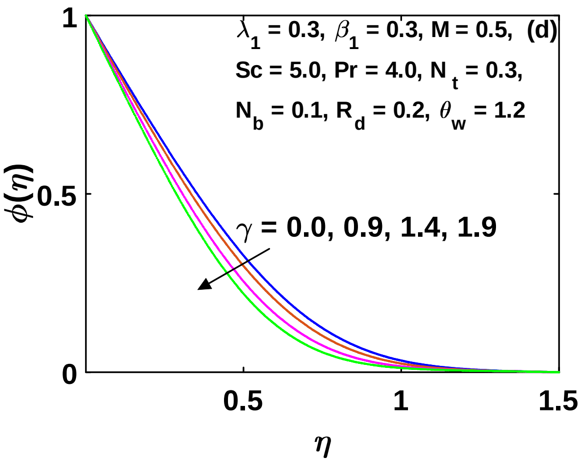

Fig. 3.3 (d) : Impression of γ on $\phi(\eta)$.

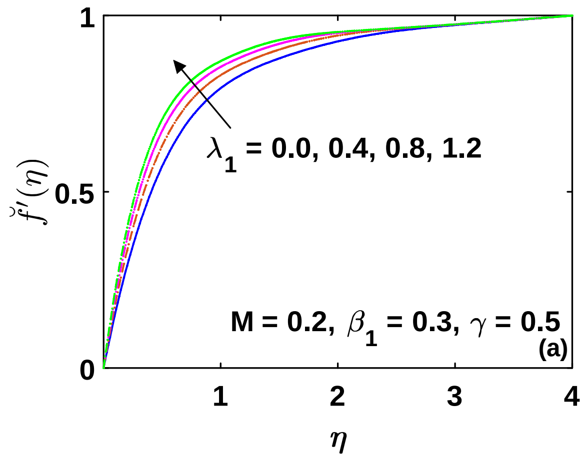

Fig. 3.4 (a) : Impression of λ_1 on $\breve{f}'(\eta)$.

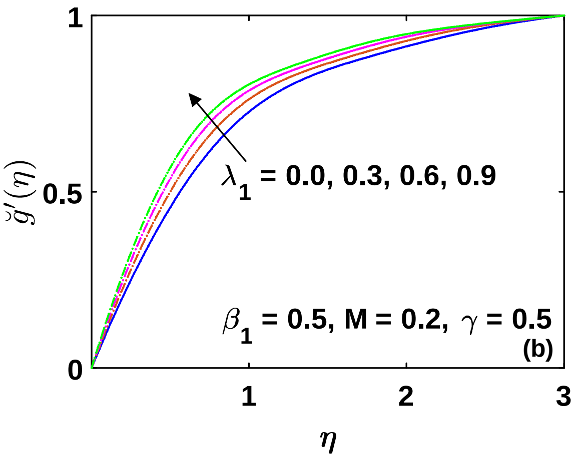

Fig. 3.4 (b) : Impression of λ_1 on $\breve{g}'(\eta)$.

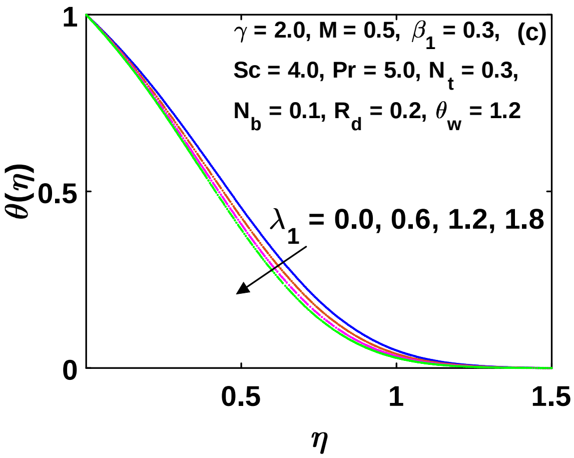

Fig. 5 (c) : Impression of λ_1 on $\theta(\eta)$.

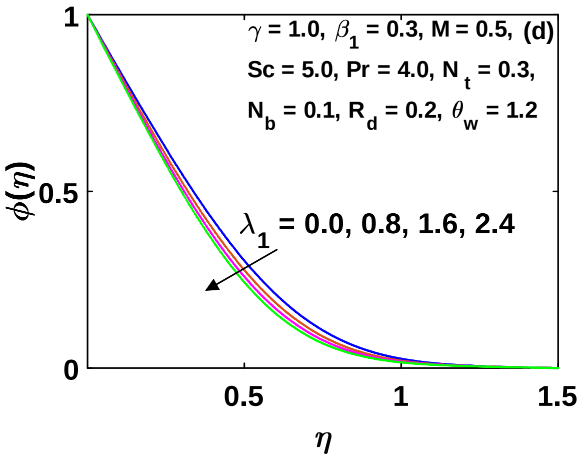

Fig. 5 (d) : Impression of λ_1 on $\phi(\eta)$.

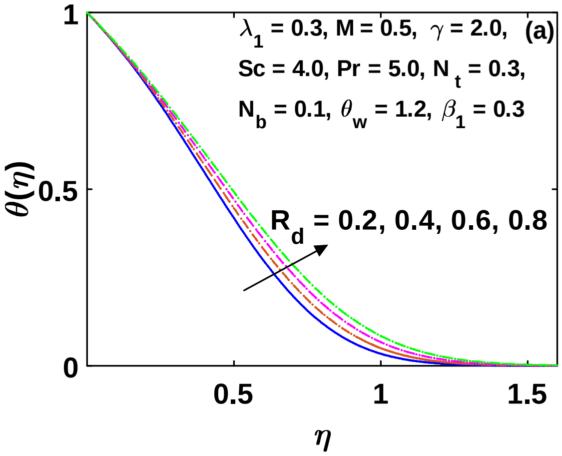

Fig. 3.5 (a) : Impression of R_d on $\theta(\eta)$.

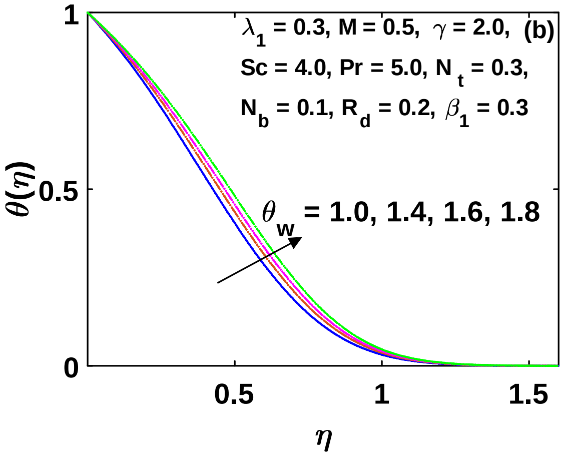

Fig. 3.5 (b) : Impression of θ_w on $\theta(\eta)$.

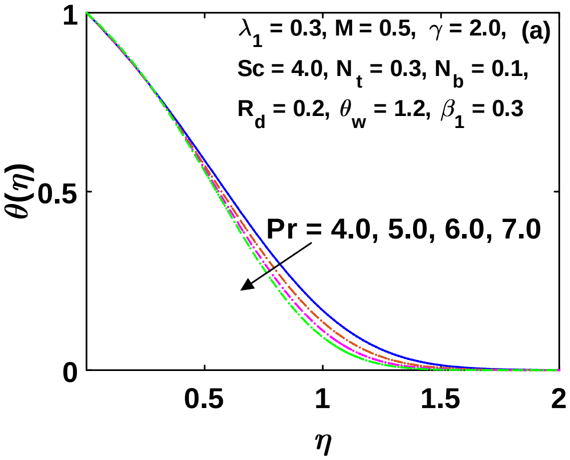

Fig. 3.6 (a) : Impression of Pr on $\theta(\eta)$.

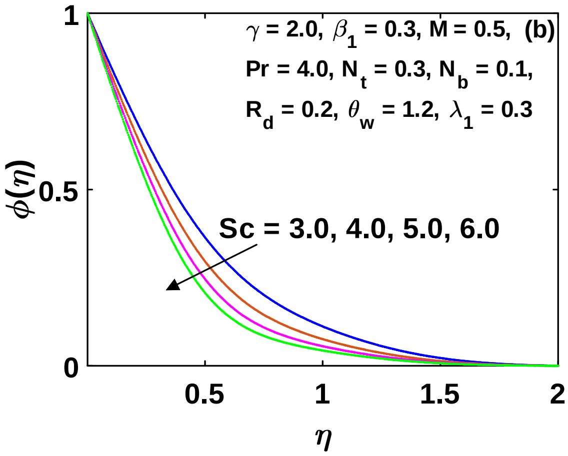

Fig. 3.6 (b) : Impression of Sc on $\phi(\eta)$.

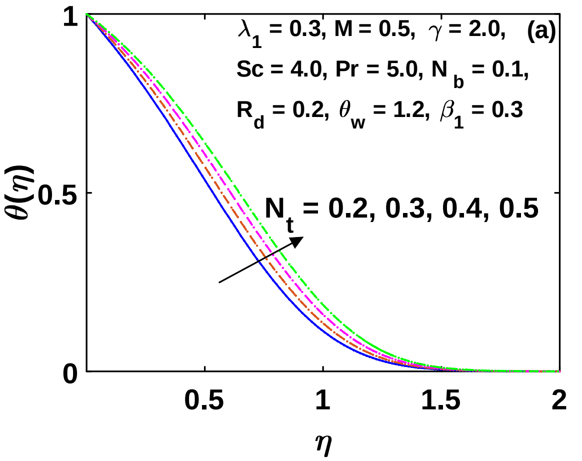

Fig. 3.7 (a) : Impression of N_t on $\theta(\eta)$.

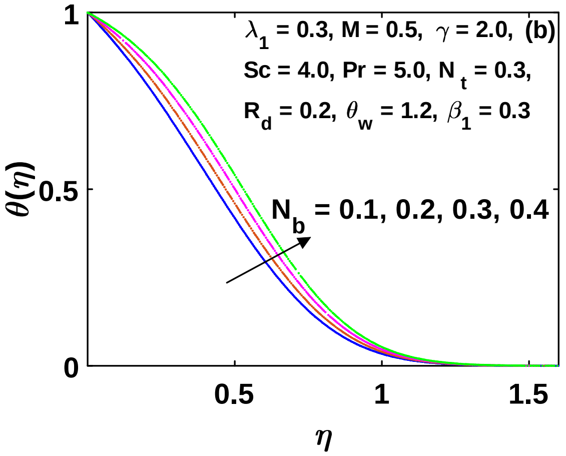

Fig. 3.7 (b) : Impression of N_b on $\theta(\eta)$.

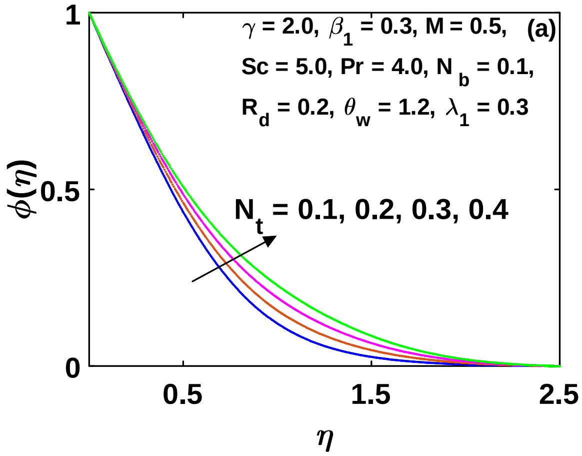

Fig. 3.7 (c) : Impression of N_t on $\phi(\eta)$.

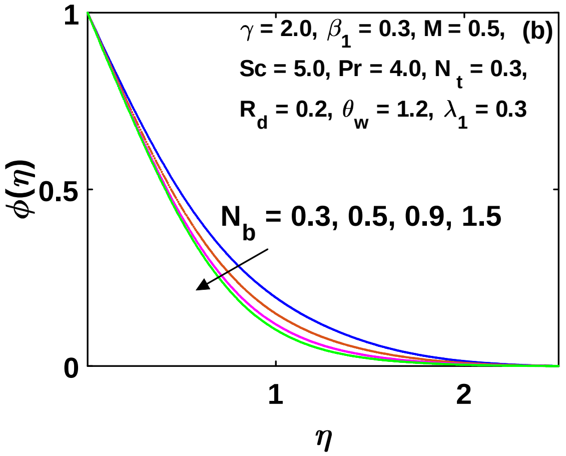

Fig. 3.7 (d) : Impression of N_b on $\phi(\eta)$.

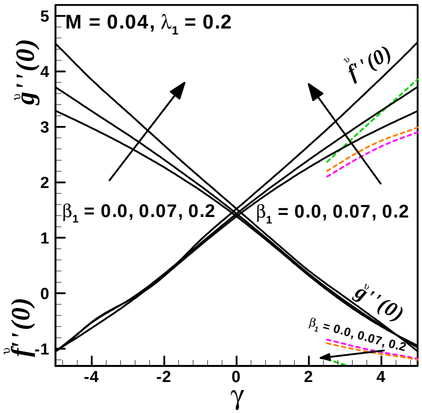

Fig. 3.8 : Impression of $\breve{f}''(0)$ and $\breve{g}''(0)$.

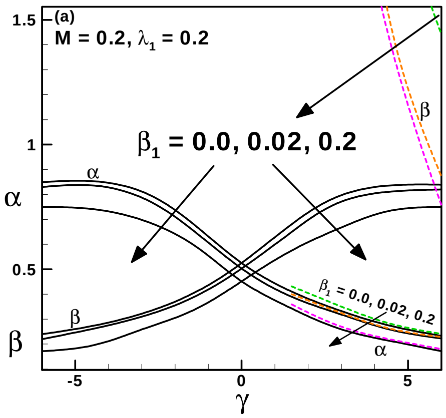

Fig. 3.9 (a) : Impression of α and β.

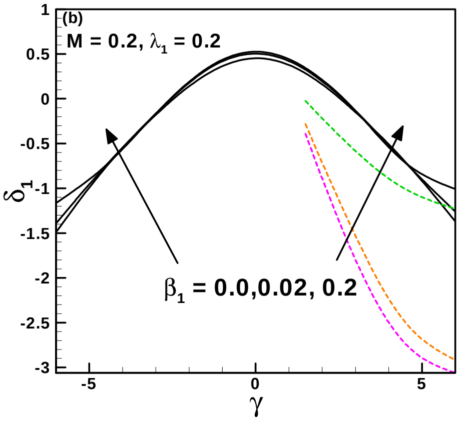

Fig. 3.9 (b) : Impression of δ_1.

3.4 Concluding Remarks

This study focused on the numerical and large-γ asymptotic solutions for Jeffrey's nanofluid flow in the stagnation-region over an electrically conducting cylindrical disk. The ramifications of the parameters involved were investigated on the fluid flow, energy, and mass transport. The numerical results and their asymptotic solutions were determined by using a built-in program, bvp4c on Matlab®. Moreover, our results were consistent with the ones in literature. The observations made are summarized below.

- The significance of Jeffrey's material parameters and magnetic field on skin drag was inspected. It is perceived that for the coefficient of skin friction along x-axis $\breve{f}''(0)$ somehow reached its asymptotic value as $\gamma \rightarrow \infty$; however, along the y-axis, the coefficient of skin friction $\breve{g}''(0)$ exhibited contrasting behavior by decaying significantly.
- The displacement thickness parameters reduced with the increment of the Deborah number for specific values of the shear-to-strain rate ratio γ. It is seen through graphs that as $\gamma \rightarrow \infty$, $\sqrt{\frac{a}{\nu}}\delta_x$ was closer to its asymptotic value; whereas, opposite behavior was depicted by $\sqrt{\frac{a}{\nu}}\delta_y$ and δ_1.
- The impact of the Lorentz force created by magnetic field caused the decay in velocity fields, while enhanced the thermal and concentration boundary layer.
- The temperature field was boosted up by the extraordinary thermal conductivity of nanofluids. However the fluid concentration was increased for the former and reduced for the latter.
- Due to the Rosseland approximation for solar radiation, the thermal boundary layer was enhanced.

Bibliography

[1] K. Walter, Non-Newtonian effects in some elastico-viscous liquids whose behavior at small rates of shear is characterized by a general linear equation of state, Q. J. Mech. Appl. Math., 15, (1962) 63–76.

[2] S. Baris, Steady three-dimensional flow of a Walter's B fluid in a vertical channel, Turkish J. Eng. Env. Sci., 26, (2002) 385–394.

[3] F. Labropulu, I. Husain. and M. Chinichian, Stagnation-point flow of the Walters' B fluid with slip, Int. J. Math. Math. Sci., 61, (2004) 3249–3258.

[4] S.A.M. Tonekaboni, R. Abkar and R. Khoeilar, On the study of viscoelastic Walter's B fluid in boundary layer flows, Math. Probl. Eng., (2012) https://doi.org/10.1155/2012/861508

[5] Q.A. Mdallal, K.A. Abro, and I. Khan, Analytical solutions of fractional Walter's B fluid with applications, Complexity, (2018) https://doi.org/10.1155/2018/8131329

[6] T.R. Mahapatra, and S. Sidui, Non-axisymmetric Homann stagnation-point flow of a viscoelastic fluid towards a fixed plate, Eur. J. Mech.-B/Fluids, 79, (2020) 38–43.

[7] A.F. Khadrawi, M.A. Al-Nimr, and A. Othman, Basic viscoelastic fluid flow problems using the Jeffreys model, Chem. Eng. Sci., 60(24) (2005) 7131–7136.

[8] N.S. Akbar, S. Nadeem, and M. Ali, Jeffrey fluid model for blood flow through a tapered artery with a stenosis, J. Mech. Med. Biol., 11(3), (2011) 529–545.

[9] M. Khan, F. Iftikhar, and A. Anjum, Some unsteady flows of a Jeffrey fluid between two side walls over a plane wall, Z. Naturforsch., 66a (12), (2011)745–752.

[10] K. Hiemenz, Die Grenzschicht an einem in den gleichfdrmingen Flussigkeitsstrom eingetauchten geraden Kreiszylinder, Dingl. J., 326, (1911) 321–410.

[11] F. Homann, Der Einfluss grosser Z¨ahigkeit bei Str¨omung um Zylinder, Z. Angew. Math. Mech., 16 (1936) 153–164.

[12] L. Howarth, The boundary layer equations in three-dimensional flow. Part II. The flow near a stagnation point, Phil. Mag., 42, (1951) 1433–1440.

[13] A. Darvey, Boundary-layer flow at a saddle point of attachment, J. Fluid Mech., 10, (1961) 593–610.

[14] V.K. Garg, Heat transfer due to stagnation point flow of a non-Newtonian fluid. Acta Mech., 104(3-4), (1994) 159–171.

[15] R. Seshadri, N. Sreeshylan, and G. Nath, Unsteady three-dimensional stagnation point flow of a viscoelastic fluid, Int. J. Eng. Sci., 35, (1997) 445–454.

[16] C.Y. Wang, Stagnation flow towards a shrinking sheet, Int. J. Nonlin. Mech., 43, (2008) 377–382.

[17] A.S. Abbassi, and A.B. Rahimi, Nonaxisymmetric three-dimensional stagnation-point flow and heat transfer on a flat plate, J. Fluids Eng., 131, (2009) 074501.

[18] P.D. Weidman, Non-axisymmetric Homann stagnation-point flows, J. Fluid Mech., 702, (2012) 460–469.

[19] P.D. Weidman, Axisymmetric stagnation-point flow on a spiraling disk, Phys. Fluids, 26, (2014) 073603.

[20] P.D. Weidman and Y.P. Ma, The competing effects of wall transpiration and stretching on Homann stagnation-point flow, Eur. J. Mech. B/Fluids, 60, (2016) 237–241.

[21] T.R. Mahapatra, and S. Sidui, Unsteady heat transfer in non-axisymmetric Homann stagnation-point flows towards a stretching/shrinking sheet, Eur. J. Mech. B/Fluids, 75, (2019) 199–208.

[22] S.U. Choi, and J.A. Eastman, Enhancing thermal conductivity of fluids with nanoparticles, Developments and Applications of Non-Newtonian Flows, FED-vol. 231/MD-vol. 66, (1995) 99–105.

[23] L. Cheng, Nanofluid heat transfer technologies, Recent Pat. Eng., 3, (2009) 1–7.

[24] J. Buongiorno, Convective transport in nanofluids, ASME J. Heat Transf., 128, (2006) 240–250.

[25] R.K. Tiwari, and M.K. Das, Heat transfer augmentation in a two-sided lid-driven differentially heated square cavity utilizing nanofluids, Int. J. Heat Mass Transf., 50, (2007) 2002–2018.

[26] K.F.V. Wong, and T. Kurma, Transport properties of alumina nanofluids, Nanotechnology, 19, (2008) 345702.

[27] S.U. Choi, Nanofluids: A new field of scientific research and innovative applications, (2008) 429–431. https://doi.org/10.1080/01457630701850778

[28] M. Chopkar, P.K. Das, and I. Manna, Synthesis and characterization of nanofluid for advanced heat transfer applications. Scr. Mater., 55, (2008) 549–552.

[29] M.U. Sajid and H.M. Ali, Recent advances in application of nanofluids in heat transfer devices: a critical review, Renew. Sust. Energ. Rev., 103, (2019) 556–592.

[30] J. Ahmed, A. Shahzad, M. Khan, and R. Ali, A note on convective heat transfer of an MHD Jeffrey fluid over a stretching sheet, AIP Adv., 5(11), (2015) 117117.

[31] S.A. Shehzad, Z. Abdullah, A. Alsaedi, F.M. Abbasi, and T. Hayat, Thermally radiative three-dimensional flow of Jeffrey nanofluid with internal heat generation and magnetic field, J. Magn. Magn. Mater., 397, (2016) 108–114.

[32] M. Farooq, M.I. Khan, M. Waqas, T. Hayat, A, Alsaedi, and M.I. Khan, MHD stagnation point flow of viscoelastic nanofluid with non-linear radiation effects, J. Mol. Liq., 221, (2016) 1097–1103.

[33] S.K. Raju, N. Sandeep, and M.G. Reddy, Effect of nonlinear thermal radiation on 3D Jeffrey fluid flow in the presence of homogeneous–heterogeneous reactions, Int. J. Eng. Res. Afr., 21, (2016) 52–68.

[34] V.R. Reddy, M.S. Reddy, N. Nagendra, A.S. Rao, and M.S. Reddy, Radiation Effect on Boundary Layer Flow of a non-Newtonian Jeffrey Fluid Past an Inclined Vertical Plate, i-Manager's J. Math., 6(2), (2017) 34.

[35] A. Hussain, L. Sarwar, S. Akbar, M.Y. Malik, and S. Ghafoor, Model for MHD viscoelastic nanofluid flow with prominence effects of radiation, Heat Transf.–Asian Res., 48, (2019) 463–482.

[36] P. Besthapu, R.U. Haq, S. Bandri, and Q.M.A. Mdallal, Thermal radiation and slip effects on MHD stagnation point flow of non-Newtonian nanofluid over a convective stretching surface, Neural Comput. Appl., 31, (2019) 207–217.

[37] M. Almakki, S.K. Nandy, S. Mondal, P. Sibanda, and D. Sibanda, A model for entropy generation in stagnation-point flow of non-Newtonian Jeffrey, Maxwell, and Oldroyd-B nanofluids, Heat Transf.–Asian Res., 48(1), (2019) 24–41.

[38] F.A. Soomro, M. Usman, R.U. Haq, and W. Wang, Melting heat transfer analysis of Sisko fluid over a moving surface with non-linear thermal radiation via Collocation method, Int. J. Heat Mass Transf., 126, (2018) 1034–1042.

[39] D.W. Beard and K.Walters, Elastico-viscous boundary-layer flows I. Two-dimensional flow near a stagnation point, Math. Proc. Camb. Philos. Soc., 60(3), (1964) 667-674.

[40] M.J. Lighthill, On displacement thickness, J. Fluid Mech., 4(4), (1958) 383–392.